JAMES | Journal of Advances in Modeling Earth Systems

RESEARCH ARTICLE
10.1029/2023MS004028

Special Collection:
The CliMA Earth System Model

# Training Warm-Rain Bulk Microphysics Schemes Using Super-Droplet Simulations

**Sajjad Azimi[1], Anna Jaruga[1], Emily de Jong[2], Sylwester Arabas[3], and Tapio Schneider[1,4]**

[1]Department of Environmental Science and Engineering, California Institute of Technology, Pasadena, CA, USA, [2]Department of Mechanical and Civil Engineering, California Institute of Technology, Pasadena, CA, USA, [3]Faculty of Physics and Applied Computer Science, AGH University of Krakow, Kraków, Poland, [4]Jet Propulsion Laboratory, California Institute of Technology, Pasadena, CA, USA

**Abstract** Cloud microphysics is a critical aspect of the Earth's climate system, which involves processes at the nano- and micrometer scales of droplets and ice particles. In climate modeling, cloud microphysics is commonly represented by bulk models, which contain simplified process rates that require calibration. This study presents a framework for calibrating warm-rain bulk schemes using high-fidelity super-droplet simulations that provide a more accurate and physically based representation of cloud and precipitation processes. The calibration framework employs ensemble Kalman methods including Ensemble Kalman Inversion and Unscented Kalman Inversion to calibrate bulk microphysics schemes with probabilistic super-droplet simulations. We demonstrate the framework's effectiveness by calibrating a single-moment bulk scheme, resulting in a reduction of data-model mismatch by more than 75% compared to the model with initial parameters. Thus, this study demonstrates a powerful tool for enhancing the accuracy of bulk microphysics schemes in atmospheric models and improving climate modeling.

**Plain Language Summary** Cloud microphysics is a complex set of processes that determine the formation and evolution of particles in clouds, which affects the Earth's climate by regulating precipitation and cloud cover. However, the vast difference in scale between the microphysics and large-scale atmospheric flows makes it impossible to simulate these processes in climate models directly. Instead, climate models use simplified methods to represent cloud microphysics, which can result in inaccuracies. In this study, we focus on calibrating the simplified models with more detailed simulations of cloud microphysics using the super-droplet method. We demonstrate a framework for calibrating the simplified models using high-fidelity simulations, which improves the accuracy of these models.

**Key Points:**

- A calibration framework for warm-rain bulk microphysics parameterizations is presented
- The framework relies on a library of super-droplet simulations of a rain shaft
- Calibrating a single-moment microphysics scheme with the calibration framework substantially reduces the model-data mismatch

**Correspondence to:**
S. Azimi,
azimi@caltech.edu

**Citation:**
Azimi, S., Jaruga, A., de Jong, E., Arabas, S., & Schneider, T. (2024). Training warm-rain bulk microphysics schemes using super-droplet simulations. *Journal of Advances in Modeling Earth Systems*, *16*, e2023MS004028. https://doi.org/10.1029/2023MS004028

Received 20 SEP 2023
Accepted 30 JUN 2024

**Author Contributions:**
**Conceptualization:** Sajjad Azimi, Anna Jaruga, Emily de Jong, Sylwester Arabas, Tapio Schneider
**Data curation:** Sajjad Azimi
**Formal analysis:** Sajjad Azimi, Anna Jaruga, Emily de Jong, Sylwester Arabas, Tapio Schneider
**Funding acquisition:** Sajjad Azimi, Tapio Schneider
**Investigation:** Sajjad Azimi, Anna Jaruga, Emily de Jong, Sylwester Arabas, Tapio Schneider
**Methodology:** Sajjad Azimi, Anna Jaruga, Emily de Jong, Sylwester Arabas, Tapio Schneider
**Project administration:** Tapio Schneider
**Resources:** Tapio Schneider



## 1. Introduction

Cloud microphysics refers to the microscale processes within clouds that control the formation and evolution of hydrometeors, such as cloud droplets, ice crystals, and raindrops. These processes are essential for regulating many mesoscale properties of clouds, such as precipitation and cloud albedo, which are important factors in the Earth's climate system. Despite the crucial role of cloud microphysics, climate models cannot resolve these processes, mainly due to the vast scale separation between the micro-scale dynamics of hydrometeors and large-scale atmospheric flows. As a result, climate models commonly represent cloud microphysics by representing particle size distributions (PSD) of hydrometeors through bulk methods. Bulk methods track the evolution of aggregate properties of the PSD, such as the total mass or number of particles. While bulk schemes are the dominant numerical approach in climate modeling, they have significant uncertainty in both the structure of the model and the parameters (Igel et al., 2022; Khain et al., 2015; Morrison et al., 2019). However, the uncertainty in the parameters can be reduced through calibration against more detailed methods such as spectral bin methods and particle-based super-droplet methods (SDMs) (e.g., Gettelman et al., 2021; Noh et al., 2018; van Lier-Walqui et al., 2020). In this paper, we will focus on calibrating parameters in bulk methods with detailed results of the particle-based SDM to improve the accuracy of climate models.

While bulk methods have the advantage of reducing the computational cost of microphysics modeling, their accuracy is limited by several factors. First, bulk methods follow the evolution of a few moments of the PSD, while many process rates depend on higher moments. Therefore, the bulk methods require closures that express higher moments in terms of the tracked moments. These closures are typically derived by assuming specific

**Software:** Sajjad Azimi, Anna Jaruga, Emily de Jong, Sylwester Arabas
**Supervision:** Tapio Schneider
**Validation:** Sajjad Azimi, Anna Jaruga, Emily de Jong, Sylwester Arabas, Tapio Schneider
**Visualization:** Sajjad Azimi
**Writing – original draft:** Sajjad Azimi
**Writing – review & editing:** Sajjad Azimi, Anna Jaruga, Emily de Jong, Sylwester Arabas, Tapio Schneider

functional forms for the size distribution, such as a gamma or exponential distribution (e.g., Khairoutdinov & Kogan, 2000; Liu & Daum, 2004; Morrison & Grabowski, 2007; Seifert & Beheng, 2006). However, in reality, the size distribution of hydrometeors can be multimodal. Consequently, bulk methods consider different particle categories, such as cloud droplets and raindrops, each represented by different unimodal distributions. The conversion rate between these categories is parameterized, leading to uncertainties in climate modeling. Furthermore, the use of multiple categories is an artificial representation of the continuous real-world physics of hydrometeors, and the conversion rates may not be able to capture the collective physics of hydrometeors well. Studies such as Kogan and Belochitski (2012), Bieli et al. (2022), and Igel et al. (2022) explore alternative approaches to avoid artificial water categories and conversion rates between them in bulk models. Second, parameterizations in bulk schemes typically include several process rate parameters that need to be calibrated with reference physics, which can be observational data or high-fidelity numerical simulations. However, despite the abundance of satellite observations available, it remains challenging to leverage them effectively for the development of microphysics schemes due to the difficulties in accurately mapping from these observations to microphysical variables (Morrison et al., 2020).

Despite their limitations, bulk methods are widely used in climate modeling due to their simplicity and low computational cost, motivating researchers to continually develop new parameterizations to improve their accuracy (e.g., Kessler, 1969; Milbrandt & Yau, 2005; Morrison & Milbrandt, 2015; Morrison et al., 2019; Tripoli & Cotton, 1980). The complexity of bulk methods depends not only on the number of prognostic moments they track but also on the number of categories, the variety of processes simulated, and the complexity of process rate equations. Regardless of the complexity of a new bulk parameterization, poorly estimated parameters can impact the performance of the entire modeling system. Therefore, careful attention must be given to this aspect of bulk method development to ensure that new parameterizations are effective and reliable. Several recent studies highlighted the application of Bayesian techniques in parameter estimation for bulk microphysics schemes. Posselt and Vukicevic (2010) and Posselt (2016) employed a Markov chain Monte Carlo algorithm to investigate the relationship between cloud microphysical parameters and deep moist convection simulations. Morrison et al. (2019) and van Lier-Walqui et al. (2020) introduced the Bayesian observationally constrained statistical-physical scheme, a flexible framework designed to learn microphysical parameter distributions through Bayesian inference. Bieli et al. (2022) proposed a bulk microphysics scheme with adjustable complexity, and presented an efficient parameter learning approach using the calibrate-emulate-sample algorithm (Cleary et al., 2021; Dunbar et al., 2021). Notably, both of these studies demonstrated learning parameters of their bulk schemes by using perfect-model experiments with data generated by the same models. Additionally, Schrom et al. (2021) applied Bayesian inference to radar observations to constrain ice growth processes, demonstrating the effectiveness of radar measurements to inform parameter estimates in ice microphysics.

Access to microphysics observations for calibration and validation of bulk schemes is often limited, making high-fidelity simulations using detailed microphysics representations a critical data source. Researchers have commonly used spectral bin methods to calibrate and evaluate bulk schemes (e.g., Gettelman et al., 2021; Khairoutdinov & Kogan, 2000; Kogan, 2013; Kogan & Belochitski, 2012; Zeng & Li, 2020). However, bin methods can be susceptible to numerical diffusion, and, in the case of modeling coalescence, they inherit the limiting assumptions necessary to derive the underlying deterministic Smoluchowski equations, both of which limit their accuracy (Grabowski et al., 2019). Another detailed method that has gained increasing attention in recent years is the particle-based SDM (Andrejczuk et al., 2010; Riechelmann et al., 2012; Shima et al., 2009). This method uses a probabilistic particle-based approach to track individual super-droplets explicitly and allows for a more realistic representation of the microphysics involved in cloud and precipitation processes. Each super-droplet is treated as an ensemble of actual particles that share the same attributes, such as size, composition and location. SDM simulations are probabilistic because they involve random sampling of the attribute space at initialization and feature Monte-Carlo representation of stochastic processes such as coagulation and breakup. Each SDM simulation yields a single realization of the system evolution, which includes tracking of each super-droplet's properties through particle processes such as aerosol activation, condensation, evaporation, collision, coalescence, and break-up.

Both bin methods and the SDM aim to provide a detailed representation of microphysical processes. However, it is crucial to acknowledge that neither method is exempt from assumptions and uncertainties, particularly regarding their collection kernels, which rely on assumptions about the physics of the evolution of drops and their populations. These assumptions are necessary for computational feasibility but introduce uncertainties.

Furthermore, both methods are often evaluated against a limited set of observational data, which may not fully capture the complexities of natural cloud and precipitation processes. Despite these challenges, the SDM offers a promising approach toward a more accurate and physically based representation of cloud and precipitation processes. Structurally, SDM's Lagrangian nature marks a fundamental advantage over bin methods. This approach nullifies numerical diffusion issues associated with bin methods by avoiding the confinement of super-particles to grid box centers or vertices and eliminating advection from one size bin to the next. Moreover, SDM inherently avoids the computational inefficiencies associated with empty bins in bin methods, as it does not predetermine bins for water content.

Unlike bulk schemes that require parameterizations of conversion rates between artificial categories, the SDM avoids such parameterizations, providing a more detailed and physically justified representation of cloud and precipitation processes. As such, the particle-based super-droplet approach has the potential to provide more realistic and detailed data for improving the accuracy of bulk schemes in simulating cloud and precipitation processes. Noh et al. (2018) employed the particle-based super-droplet approach to evaluate several bulk parameterizations for collisional growth in shallow cumulus clouds. However, their study is limited to few simulations initialized with a single thermodynamic condition and excludes considerations of raindrop breakup and evaporation.

Here, we present a framework for calibrating warm-rain bulk schemes using high-fidelity super-droplet simulations. We implement the one-dimensional kinematic driver (KiD-1d) model (Shipway & Hill, 2012), and generate a library of super-droplet simulations in this model. The KiD-1d model is a one-dimensional warm rain shaft model with a prescribed flow field and constant temperature profile. The flow and temperature fields are prescribed to isolate microphysics processes from their feedbacks with dynamics and thermodynamics, enabling us to calibrate and validate microphysics schemes with consistent dynamics. This means that any variations in the results can only be attributed to changes in microphysics schemes. We utilize ensemble Kalman methods, including Ensemble Kalman Inversion (EKI) (Iglesias et al., 2013) and Unscented Kalman Inversion (UKI) (Huang et al., 2022), to calibrate bulk microphysics schemes with the super-droplet simulations. EKI and UKI are ensemble-based gradient-free methods that have demonstrated remarkable success in a wide variety of calibration studies (e.g., Dunbar, Howland, et al., 2022; Kovachki & Stuart, 2019; Xiao et al., 2016). EKI is more robust than UKI concerning noise in observations, while UKI provides parameter uncertainties and allows for model error quantification (Lopez-Gomez et al., 2022). We demonstrate the application of the calibration framework by calibrating a single-moment warm-rain bulk scheme, targeting parameters of conversion rates such as condensation, auto-conversion, accretion, sedimentation, and evaporation rates. Remarkably, calibrations using EKI and UKI obtain two different sets of optimal parameters, both resulting in a similar reduction of model-data mismatch. The difference between these two parameter sets is supported by parameter relationships revealed through parameter correlation analysis by UKI. Through our calibration process, we achieve a significant enhancement in the accuracy of the bulk model by more than 75% compared to the model with initial parameter values.

The calibration framework presented here has several notable properties compared to previous studies, such as Khairoutdinov and Kogan (2000), Morrison et al. (2019), and Gettelman et al. (2021). First, we employ the SDM as a tool capable of providing a physically based representation of microphysics for generating benchmark simulations. Second, the framework offers an efficient setup to calibrate and evaluate bulk methods by using a diverse set of rain shaft simulations with a wide variety of precipitation conditions. Finally, by using ensemble Kalman methods, which are gradient-free (meaning they do not require the computation of derivatives, making the training process simpler and more robust), we ensure both efficient parameter learning and the ability to quantify parameter uncertainties and model error. The calibration framework presented in this study provides a promising tool for enhancing the accuracy of bulk microphysics schemes in atmospheric models, with potential implications for improving climate modeling.

The manuscript is organized as follows: Section 2 provides an overview of the KiD-1d model, along with a discussion of the SDM used to generate simulations of the KiD-1d model. The section also describes the calibration methods employed in our framework for calibrating bulk schemes. In Section 3, we present a library of super-droplet simulations of the KiD-1d model and report the results of calibrating a single-moment bulk scheme using this library of rain shaft simulations. Finally, Section 4 summarizes our findings and provides an outlook for future research.

**Table 1**
*Data Points for Interpolating the Initial Water Vapor Mixing Ratio $r_{v,0}$ and Potential Temperature $\theta$*

| Height (m) | $r_{v,0}$ (kg kg$^{-1}$) | $\theta$ (K) |
|---|---|---|
| 0 | 0.015 | 297.9 |
| 740 | 0.0138 | 297.9 |
| 3,260 | 0.0024 | 312.66 |

## 2. Methods

This section provides an overview of the methods employed in this study. We describe the one-dimensional rain-shaft model, which serves as a testbed for calibrating and evaluating warm-rain bulk schemes in relation to high-fidelity particle-based simulations. Subsequently, we discuss the SDM utilized to generate a comprehensive library of simulations for benchmarking bulk schemes. Next, we present a specific example of a single-moment warm-rain bulk scheme used to demonstrate the application of the calibration framework. Lastly, we explain the calibration methods employed to refine and optimize the bulk scheme.

### 2.1. System: One-Dimensional Kinematic Driver Model

The calibration framework utilizes an implementation of the one-dimensional kinematic driver (KiD-1d) model as a testbed for calibrating and evaluating warm-rain bulk schemes. The KiD-1d model is specifically designed to facilitate the assessment of microphysics parameterizations by prescribing both the velocity and temperature fields (Hill et al., 2023; Shipway & Hill, 2012). This prescription effectively prevents any feedback from microphysics processes on dynamics and thermodynamics, thereby also preventing any subsequent feedback loop back to microphysics. This ensures that observed variations in the results can be solely attributed to changes in microphysics parameterizations. In the employed implementation of the KiD-1d model, we consider a stratified air density profile, and thus prescribe the flow by using an air momentum profile, unlike Hill et al. (2023) where a constant density is used.

The KiD-1d model represents shallow convection in a column of moist air over a height range of 3 km from the ground level. The prescribed flow field represents an updraft, which is uniform in height $z$ and sinusoidal in time $t$, as given by the equation

$$\rho w(z, t) = (\rho w)_0 \sin(\pi t/t_1), \quad 0 < t < t_1. \tag{1}$$

Here, $\rho$ represents the dry-air density, $w$ denotes the vertical velocity component, and $(\rho w)_0$ is the maximum updraft momentum. The parameter $t_1$ represents the duration of the updraft. Beyond $t_1$, there is no updraft, and $\rho w$ remains at 0. This updraft motion lifts moist air to higher, colder levels, facilitating condensation of water vapor and cloud formation. The initial vapor mixing ratio $r_{v,0}$ and the potential temperature $\theta$ are represented as piecewise linear profiles interpolated from data points provided in Table 1. The initial temperature profile $T(z)$ at $t = 0$ is computed from the potential temperature $\theta(z)$ and is held constant throughout the simulations.

For a typical resolution, a KID-1d simulation features four orders of magnitude fewer spatial points compared to a standard resolution three-dimensional large-eddy simulation, resulting in significantly enhanced computational efficiency. This efficiency makes KID-1d simulations particularly well suited for our microphysics calibrations, which require numerous simulations of the system.

### 2.2. Particle-Based Simulation Method

To generate a library of particle-based simulations of the KiD-1d model, we use the PySDM package (Bartman, Bulenok, et al., 2022; de Jong et al., 2023). PySDM is a Python-based code designed to run particle-based simulations of clouds and precipitation using super-droplets. Each super-droplet corresponds to multiple particles sharing the same properties, including size and composition, with their location being tracked explicitly while their process rates are calculated for the gridbox in which they are located. The multiplicity of a super-droplet indicates the number of actual particles it represents. For further details on the models employed in PySDM, refer to Bartman, Bulenok, et al. (2022) and de Jong et al. (2023).

While the SDM provides detailed and physically grounded results, it has several notable limitations. The treatment of collision-coalescence processes relies on the geometric collection kernel (Berry, 1967), which involves simplifying assumptions about droplet interactions. Additionally, the pragmatic grouping of real particles into super-droplets, aimed at balancing detailed representation against computational feasibility, introduces additional uncertainties. Furthermore, due to representing microphysical behavior with fewer particles, the inherent

variability among different realizations produced by the SDM is larger than that occurring in nature (Morrison et al., 2020). Moreover, many microphysical processes (e.g., drop breakup) are poorly understood, presenting a challenge for all microphysics models, including SDM.

Because the particle-based simulations are inherently stochastic, we generate 100 simulations for each configuration to determine the mean and variability of the results used for calibration purposes. In each simulation, we utilize an average of $N_{sd} = 512$ super-droplets per grid box, with a grid spacing of $dz = 50$ m and a time step of $dt = 5$ s. The Python-based code PyMPDATA (Bartman, Banaśkiewicz, et al., 2022) is used for solving the advection equation. We study the independence of the results from the chosen numerical values by performing simulations with doubled $N_{sd}$, halved $dz$, and halved $dt$. The results from these simulations show excellent agreement with the original findings, indicating that the numerical values employed are sufficient to ensure numerical accuracy of the results. (For more detailed information, see Appendix A.)

### 2.3. Single-Moment Warm-Rain Bulk Scheme

To demonstrate the application of our calibration framework, we focus on calibrating and evaluating a single-moment warm-rain bulk scheme. Specifically, we examine the single-moment bulk scheme implemented in CloudMicrophysics.jl, an open-source Julia package developed and utilized within the CliMA project (clima.caltech.edu). This bulk scheme is based on the original concept introduced by Kessler (1969). It divides the total water content into three categories: water vapor, cloud water, and rainwater. The conversion of water vapor into cloud water occurs through condensation. The conversion of cloud water to rainwater involves two processes: auto-conversion, accounting for the collision and coalescence of droplets in the cloud phase to form raindrops, and accretion, representing the collection of cloud droplets by raindrops. The sedimentation of raindrops causes them to descend to subsaturated regions, leading to the partial conversion of rainwater back into water vapor through evaporation. It is worth noting that, within this scheme, rainwater can be produced only through auto-conversion and accretion from cloud water; it cannot be produced through condensation alone.

The auto-conversion rate is represented as the ratio of the specific content of cloud water to the auto-conversion time scale. This time scale is determined by a power-law function of the cloud droplet number density ($N_d$). The auto-conversion rate is expressed as follows:

$$\left.\frac{\partial q_r}{\partial t}\right|_{acnv} = -\left.\frac{\partial q_c}{\partial t}\right|_{acnv} = \frac{q_c}{\tau_{acnv,\,0}}\left(\frac{N_d}{100\,\mathrm{cm}^{-3}}\right)^{-\alpha_{acnv}}. \tag{2}$$

In this equation, $q_c$ and $q_r$ represent the specific content of cloud and rainwater, respectively. The constant $\tau_{acnv,\,0}$ denotes the reference auto-conversion time scale, and $\alpha_{acnv}$ represents the power law parameter of the number density. This representation of the auto-conversion rate is effectively a power law function of $q_c$ and $N_d$, which is consistent with the parameterization of Khairoutdinov and Kogan (2000), among others. In this study, the aerosol number density, $N_a$, is directly mapped to the cloud droplet number density, $N_d$, bypassing aerosol activation parameterizations. Thus, the auto-conversion rate is computed based on the prescribed aerosol concentration $N_a$.

The process rate equations provided in the CloudMicrophysics.jl package are based on the following assumptions regarding the raindrop size distribution $dN/dr$, mass $m$, area $a$, and terminal velocity $v$ as functions of the particle radius $r$:

$$dN/dr = n_0 \exp(-\lambda r) \tag{3}$$

$$m(r) = m_0\left(\frac{r}{r_0}\right)^3 \tag{4}$$

$$a(r) = a_0\left(\frac{r}{r_0}\right)^2 \tag{5}$$

$$v(r) = \chi_v\, v_0 \left(\frac{r}{r_0}\right)^{1/2+\Delta_v}, \tag{6}$$

where $r_0$ denotes the reference raindrop radius used for nondimensionalization. The values of the reference raindrop mass $m_0$, area $a_0$, and terminal velocity $v_0$ are calculated as follows: $m_0 = (4/3)\,\pi\,\rho_w\,r_0^3$, $a_0 = \pi\,r_0^2$, and

$$v_0 = \left(\frac{8\left(\rho_w/\rho_m - 1\right) g\, r_0}{3\, C_d}\right)^{1/2}. \tag{7}$$

Here, $\rho_w$ represents the density of water, $\rho_m$ is the moist-air density, $g$ denotes the acceleration due to gravity, and $C_d$ is a constant drag coefficient. The coefficients $\chi_v$ and $\Delta_v$ represent the terminal velocity coefficients and are free parameters that can be adjusted during model calibration. The parameters $n_0$ and $\lambda$ serve as distribution parameters. Integrating the mass of particles over the distribution, we obtain the following equation for $\lambda$:

$$\lambda = \left(\frac{4\,\pi\,\rho_w\,n_0\,\Gamma(4)}{3\,q_r\,\rho_m}\right)^{\frac{1}{4}}, \tag{8}$$

where $\Gamma$ denotes the gamma function. The condensation of water vapor is modeled by relaxing the excess of water vapor toward the saturation specific humidity over the condensation time scale:

$$\left.\frac{d\,q_c}{dt}\right|_{cond} = \frac{q_v - q_v^*}{\tau_{cond}}, \tag{9}$$

where $q_v$ represents the specific humidity, $q_v^*$ is the saturation specific humidity, and $\tau_{cond}$ represents the time scale of condensation. The accretion rate is obtained by integrating the rate of collection of cloud droplets by raindrops while falling at their terminal velocity over the assumed raindrop size distribution. This collection rate is represented by $\chi_a E_{cr} q_c a(r) v(r) (r/r_0)^{\Delta_a}$, where $E_{cr}$ denotes the collision efficiency between cloud droplets and raindrops, and $\chi_a$ and $\Delta_a$ are the accretion coefficients that can be adjusted during the model's calibration process. The accretion rate is expressed as follows:

$$\left.\frac{d\,q_r}{dt}\right|_{accr} = -\left.\frac{d\,q_c}{dt}\right|_{accr} = n_0\,\Pi_{a,v}\,q_c\,E_{cr}\,\Gamma(\Sigma_{a,v}+1)\,\frac{1}{\lambda}\left(\frac{1}{r_0\lambda}\right)^{\Sigma_{a,v}}, \tag{10}$$

where $\Pi_{a,v} = a_0\,v_0\,\chi_a\,\chi_v$, and $\Sigma_{a,v} = 5/2 + \Delta_a + \Delta_v$. The sedimentation of rain is accounted for by the following equation, which describes the fall speed of $q_r$:

$$v_t = \chi_v\,v_0\left(\frac{1}{r_0\,\lambda}\right)^{1/2+\Delta_v}\frac{\Gamma(9/2+\Delta_v)}{\Gamma(4)}. \tag{11}$$

Finally, the rate of rain evaporation is modeled by integrating the evaporation of individual particles over the spectrum of raindrops. This leads to the following expression:

$$\begin{aligned}\left.\frac{dq_r}{dt}\right|_{evap} &= \frac{4\pi n_0}{\rho_m}(S-1)G(T)\lambda^{-2} \\ &\times\left[a_{vent} + b_{vent}\left(\frac{\nu_a}{D_v}\right)^{\frac{1}{3}}\left(\frac{1}{r_0\,\lambda}\right)^{\frac{\nu_e+\Delta_v}{2}}\left(\frac{2\chi_v\,v_0}{\nu_a\,\lambda}\right)^{\frac{1}{2}}\Gamma\left(\frac{11}{4}+\frac{\Delta_v}{2}\right)\right].\end{aligned} \tag{12}$$

In this equation, $S = q_v/q_v^*$ represents the saturation, $T$ denotes the temperature, $D_v$ is the diffusivity of water vapor, $\nu_a$ is the kinematic viscosity of air, and $a_{vent}$ and $b_{vent}$ are ventilation parameters. The function $G(T)$ is defined as:

$$G(T) = \left(\frac{L}{k\,T}\left(\frac{L}{R_v\,T}-1\right) + \frac{R_v\,T}{p_v^*\,D_v}\right)^{-1} \tag{13}$$

**Table 2**
*Parameters of the Single-Moment Bulk Scheme*

| Parameter name | Description | Value |
|---|---|---|
| $*\tau_{cond}$ | Condensation time scale | 10 s, KM2003 |
| $*\tau_{acnv,\,0}$ | Auto-conversion time scale | 1,000 s, GS1996 |
| $*\alpha_{acnv}$ | Auto-conversion coefficient | 1, LD2004 |
| $*\chi_v$ | Terminal velocity coefficient | 1 |
| $*\Delta_v$ | Terminal velocity coefficient | 0 |
| $*\chi_a$ | Accretion coefficient | 1 |
| $*\Delta_a$ | Accretion coefficient | 0 |
| $a_{vent}$ | Evaporation coefficient | 1.5, GS1996 |
| $*b_{vent}$ | Evaporation coefficient | 0.53, GS1996 |
| $r_0$ | Reference raindrop radius | $10^{-3}$ m |
| $n_0$ | Size distribution parameter | $16 \cdot 10^6$ m$^{-4}$, MP1948 |
| $C_d$ | Raindrop drag coefficient | 0.55, GS1996 |
| $E_{cr}$ | Collision efficiency | 0.8, G1998 |

*Note.* The columns show parameter names, brief descriptions, and prior values with references. The references are KM2003 (Korolev & Mazin, 2003), GS1996 (Grabowski & Smolarkiewicz, 1996), and LD2004 (Liu & Daum, 2004), MP1948 (Marshall & Palmer, 1948), and G1998 (Grabowski, 1998). Note that the values of $a_{vent}$ and $b_{vent}$ are determined to achieve a close agreement with the evaporation rate of GS1996 at a specific humidity of 15 g/kg and $T = 288$ K. Additionally, the value of $C_d$ is chosen to closely approximate the terminal velocity of GS1996. Parameters selected for calibration are indicated by an asterisk preceding their names.

where $L$ is the latent heat of vaporization, $k$ is the thermal conductivity of air, $R_v$ is the gas constant of water vapor, and $p_v^*$ represents the saturation vapor pressure.

The single-moment bulk scheme considered in this study involves several notable simplifications. First, the functional form of the auto-conversion parameterization is straightforward, representing it as the ratio of available cloud water to an auto-conversion time scale. Second, the scheme assumes that the distribution of raindrops follows an exponential distribution, characterized by a constant scaling parameter $n_0$. Third, in the parameterization of terminal velocity, a constant drag coefficient is employed, which is assumed to apply uniformly to all particles, while in reality, the drag coefficient is a function of raindrop size. Finally, the scheme adopts a constant collision efficiency in the parameterization of accretion rate. These simplifications, while enhancing computational efficiency, can affect the model's performance.

Table 2 provides a list of parameters of the single-moment bulk method, along with their prior values. We select a subset of the parameters for calibration, specifically focusing on those that do not have easily definable physical values. These choices aim to comprise a set of parameters that uniquely govern auto-conversion, accretion, the terminal velocity of raindrops, and the rain evaporation rate. To ensure coverage of these processes, we selected one or two parameters from each process, each capable of significantly modifying that specific process. Specifically, we select $\tau_{cond}$ to represent the condensation process, $\tau_{acnv\ 0}$ and $\alpha_{acnv}$ for auto-conversion, $\chi_v$ and $\Delta_v$ for raindrop terminal velocity, and $\chi_a$ and $\Delta_a$ for accretion. Additionally, we include $b_{vent}$ to regulate the rate of evaporation. Other parameters of the model that are modulated by the calibrated parameters remain constant during model calibration. For instance, $n_0$ is held constant because the product of $\chi_a$ and $n_0$ governs the accretion rate, and we choose to calibrate $\chi_a$.

### 2.4. Algorithms for Learning Parameters

The problem of learning parameters for the bulk method is formulated as an inverse problem, represented by the equation

$$y = \mathcal{H} \circ \Psi \circ \mathcal{T}^{-1}(\theta) + \delta + \eta. \tag{14}$$

Here, $y$ represents the vector of observations, and $\theta$ represents the vector of learnable parameters, which are transformed into an unconstrained space $\theta \in \mathbb{R}^p$. The operator $\mathcal{T}$ is a transformation map that converts parameters $\phi$ from their constrained subspace (where they satisfy constraints such as positivity) to the unconstrained space, such that $\theta = \mathcal{T}(\phi)$. The mapping $\Psi$ represents the dynamical model, while $\mathcal{H}$ denotes the observational map incorporating necessary post-processing operations to generate model predictions aligned with the observations. For example, $y$ may represent averaged specific water content data from particle-based simulations, $\Psi$ represents bulk scheme simulation results, and $\mathcal{H}$ could involve spatial and temporal averaging. The observational noise associated with the observations $y$ is indicated by $\eta$, and the model error by $\delta$. Both $\eta$ and $\delta$ are assumed to follow a Gaussian distribution with zero mean.

To ensure the generalizability of the calibrated model, we train it using multiple system configurations, which include various setups of the KiD-1d model with differences in the updraft amplitude and initial aerosol number density. We refer to the set of system configurations used for model training as $C$. In this study, $|C| = 49$ configurations are used for the calibrations. The observation vector $y$ consists of observations obtained from all system configurations: $y = \left[y_1, y_2, \ldots, y_{|C|}\right]^T$. For each system configuration, 100 SDM simulations are conducted, and the mean values of specific contents of cloud water, rainwater, and water vapor over intervals of

100 m and 10 min are extracted. The data are then normalized by dividing each field by the maximum of its standard deviation across the 100 simulations. Subsequently, the observation vector $y_c$ and the noise covariance $\Gamma_c$ are computed for each configuration $c$ using the normalized data obtained from the 100 SDM simulations.

To calibrate the parameters of the bulk scheme using particle-based simulations, we employ two gradient-free algorithms available in the EnsembleKalmanProcesses.jl package (Dunbar, Lopez-Gomez, et al., 2022): EKI and UKI. These algorithms, derived from the extended Kalman filter, heavily rely on Gaussian conditioning, which involves approximating the parameter distributions as Gaussian for the derivation of their update rules. EKI utilizes an iterative procedure to search for the optimal parameter set (maximum a posteriori, MAP, or maximum likelihood estimator, MLE, if Bayesian regularization is not applied (Lopez-Gomez et al., 2022)) by updating an ensemble of $J$ parameter sets with $J \sim p$. For our calibrations, we choose $J = 20$. The initial ensemble is formed by randomly sampling parameters from a Gaussian distribution. On the other hand, UKI adopts a deterministic approach to update an initial Gaussian estimate represented by an ensemble of $J = 2p + 1$ parameter sets, aiming to approximate the posterior distribution around the MAP or the likelihood centered around the MLE. EKI shows greater robustness against observation noise than UKI, while UKI quantifies model error and estimates parameter uncertainties. For a detailed discussion on both algorithms, refer to Lopez-Gomez et al. (2022). It is important to note that, while both EKI and UKI have the capability to estimate the MAP through Bayesian regularization, our application does not leverage this aspect. Instead, our approach concentrates on maximizing the likelihood to find the optimal parameter sets that best fit our data. For EKI, the "optimal parameter set" refers to the convergence point of the parameter ensemble, and for UKI, it refers to the mean of the obtained parameter distribution, which, due to the Gaussian approximation, coincides with its mode.

The primary challenge with EKI and UKI is their derivation under assumptions that the dynamical model can be linearly approximated and the observational noise is Gaussian (Bocquet et al., 2010). Despite these assumptions, EKI and UKI have proven effective in nonlinear and non-Gaussian settings (e.g., Dunbar, Howland, et al., 2022; Lopez-Gomez et al., 2022). Their gradient-free nature allows for flexibility in handling discontinuities in the dynamical model, although fully addressing processes with sharp thresholds remains a challenge. Another concern is enforcing parameter constraints, such as positivity, which can be mitigated through the use of transformation maps. These maps convert parameters from their original constrained spaces to unconstrained spaces, enabling Gaussian distribution assumptions while retaining physically meaningful bounds. Notably, for high-dimensional systems the ensemble size requirement of $J \sim p$ could render EKI impractical; UKI faces even greater challenges, requiring an ensemble size of $J = 2p + 1$. Recent studies, such as the localized EKI, demonstrate the feasibility of solving high-dimensional inverse problems with a modest ensemble size (Tong & Morzfeld, 2023). This approach is inspired by localization techniques in ensemble data assimilation methods that are commonly used in weather forecasting to estimate millions of unknowns with an ensemble size of just a few hundred (e.g., Ott et al., 2004). In our study, an ensemble size of $J = 20$ for EKI is found to be practical and effective.

Training the model involves minimizing the average configuration loss function that penalizes the mismatch between observations and model outputs. The average configuration loss is given by

$$L(\theta; y) = \frac{1}{2|C|} \sum_{c=1}^{|C|} \| y_c - \mathcal{H}_c \circ \Psi_c \circ \mathcal{T}^{-1}(\theta) \|_{\Gamma_c}^2, \tag{15}$$

where $\|.\|_{\Gamma_c}$ represents the Mahalanobis norm, with $\|.\|_{\Gamma_c}^2 = \langle \cdot, \Gamma_c^{-1} \cdot \rangle$. Both EKI and UKI require evaluating the loss at each iteration, which involves running the model for all configurations. However, this can be computationally expensive. To address this, we employ mini-batches of configurations denoted as $B \subset C$ to approximate the average configuration loss:

$$L(\theta; y_B) = \frac{1}{2|B|} \sum_{c \in B} \| y_c - \mathcal{H}_c \circ \Psi_c \circ \mathcal{T}^{-1}(\theta) \|_{\Gamma_c}^2. \tag{16}$$

Batching is a commonly used technique that helps prevent convergence to local minima and thus improves generalization (Li et al., 2014). For our study, we choose a batch size of $|B| = 6$ for running the calibrations. During model training, EKI and UKI receive data from a mini-batch of $|B|$ configurations at each iteration. The

mini-batches are randomly drawn without replacement from the set of training configurations $C$. An epoch corresponds to a complete cycle through all available configurations such that no other mini-batch can be composed of the remaining configurations. At the end of each epoch, the configurations are reshuffled. With $|C| = 49$ and $|B| = 6$, each epoch consists of eight iterations.

The initial parameter ensembles for both EKI and UKI are determined randomly, centered around the prior means. Standard deviations are set to 20% of the prior means for parameters where the prior mean is nonzero. For the parameters $\Delta_a$ and $\Delta_v$, with a prior mean of zero, standard deviations are set to 0.4 and 0.1, respectively.

## 3. Results and Discussion

In this section, first, we discuss a library of particle-based simulations of the KiD-1d model for different system configurations. Then, we continue by demonstrating the calibration of the single-moment bulk scheme using the library of particle-based simulations as a benchmark.

### 3.1. Library of Rain Shaft Simulations

We have generated a library of KiD-1d model simulations using the SDM. This library includes simulations with varying values of the updraft amplitude ($(\rho w)_0$), initial aerosol number density ($N_a$), and ground-level pressure ($p_0$). The updraft amplitude ranges from 1.0 kg m$^{-2}$ s$^{-1}$–4.0 kg m$^{-2}$ s$^{-1}$ in increments of 0.5 kg m$^{-2}$ s$^{-1}$. The initial aerosol number density takes values of $N_a$ = [10, 20, 50, 100, 200, 500, 1,000] cm$^{-3}$, all corresponding to concentration at standard temperature and pressure conditions for dry air. The aerosol concentrations are selected to span conditions from very clean to heavily polluted atmospheres, ensuring the robustness of our calibration across a wide range of aerosol conditions. Simulations are conducted for five different surface air pressures, ranging from $p_0$ = 988 hPa to $p_0$ = 1,012 hPa in increments of 6 hPa. Each increment in air pressure corresponds to an approximate increase of 0.5 K in the prescribed temperature profile, which impacts the cloud condensate profile. For each combination of variables, we produce 100 simulations to compute the average and variability of the results.

By varying the values of the updraft speed and surface pressure, we can influence the amount of condensed cloud water and, consequently, the precipitation. Additionally, changing the initial aerosol number density influences the collision and coalescence of droplets, thereby influencing the formation of rain (Tao et al., 2012). The selection of different values for these control parameters allows us to generate various rain formation conditions. This variety is crucial for providing the calibration process with diverse training data, thus enhancing the generalizability of the trained model.

In addition to the simulations of the KiD-1d model involving all processes, we conducted additional simulations where the collision and coalescence processes were excluded. These simulations, referred to as condensation-only cases, do not result in rain formation as droplets do not grow large enough to sediment through condensation alone. We performed these simulations with the intention of using them as a reference to evaluate the numerical advection of ambient moisture and the condensation scheme of the bulk model separately from other process parameterizations. Figure 1 (left panels) illustrates an example simulation of a condensation-only case. The figure shows the height-time contours of the cloud water and rainwater specific content, as well as the cloud water path (CWP), rainwater path (RWP) and surface rain rate (RR) over time. The CWP and RWP represent the total amount of cloud water and rainwater in a column of moist air per unit area, respectively. As is evident in Figure 1 (left panels), condensation primarily occurs within the first 10 min of the simulation ($t < t_1$) when the updraft speed is non-zero. After $t_1$ = 10 min, no rainwater forms as collision and coalescence processes are not considered, and the cloud water is preserved.

When collision and coalescence processes are involved, formation of raindrops is observed. We use a fixed radius threshold of 50 μm to differentiate raindrops from cloud droplets for simulation output analysis. We found the sensitivity of the results to the exact value of this threshold to be insignificant. Figure 1 (right panels) illustrates the generation of rain in the simulation of the KiD-1d model with the inclusion of rain production through particle collision and coalescence. Following the coalescence of particles and the formation of raindrops, the raindrops descend due to sedimentation, moving below the cloud base where water vapor is not saturated. Consequently, rain evaporation occurs, resulting in only some of the initial rain water reaching the surface.

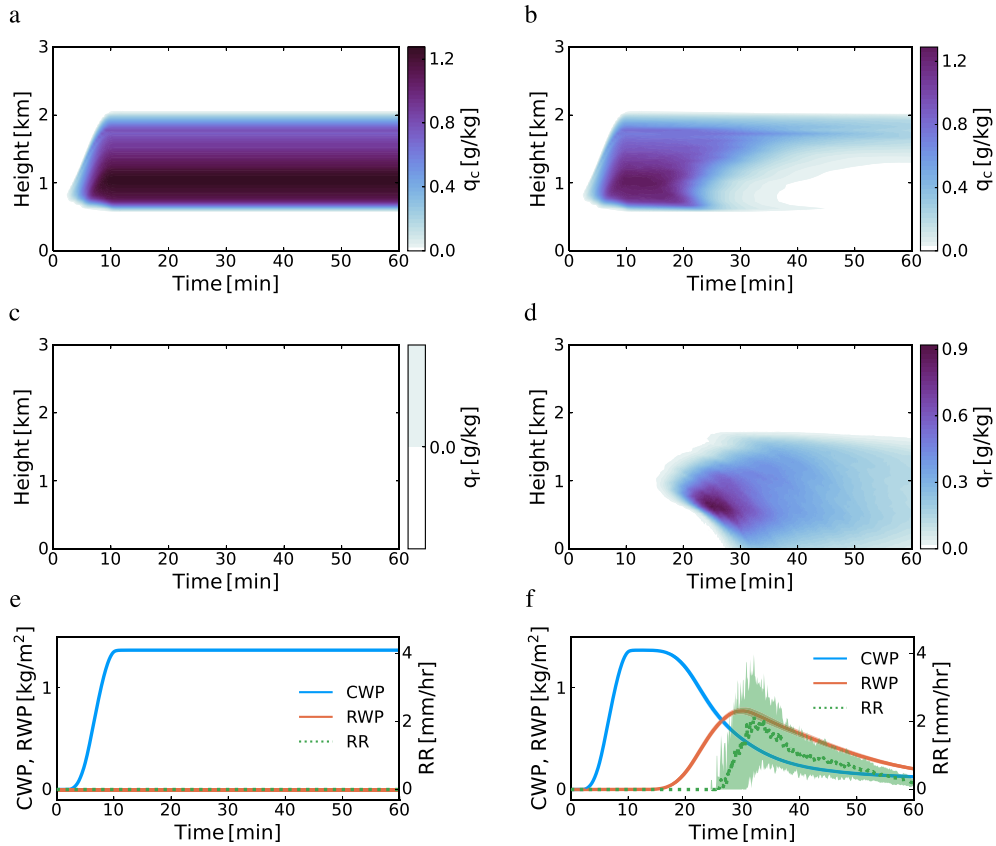


**Figure 1.** Simulations of the KiD-1d model using the super-droplet method, both without (left panels) and with (right panels) the inclusion of rain production through particle collision and coalescence. The simulations employ an updraft momentum amplitude of 3 kg m$^{-2}$ s$^{-1}$ and an initial aerosol number density of 100 cm$^{-3}$. Height-time contours for the average specific cloud water content, $q_c$ (a and b), as well as the average specific rainwater content, $q_r$ (c and d) are shown. Panels (e and f) illustrate the evolution over time of cloud water path, rainwater path, and surface rain rate. In panel (f), variations in the graphs are represented by shading, indicating one standard deviation above and below the mean.

Varying the updraft speed and aerosol number density impacts precipitation processes by influencing the availability of water vapor for condensation and the number of particles contributing to rain formation through collision and coalescence. Increases in updraft speed enhance supersaturation and cloud water content, thereby leading to increased rain production. Conversely, higher aerosol concentrations lead to the formation of smaller droplets, reducing the efficiency of collision-coalescence and, consequently, rain production (Lohmann et al., 2016). Figure 2 illustrates these effects in the context of KiD-1d simulations with a fixed surface pressure of $p_0$ = 1,000 hPa. It demonstrates that the maximum CWP (Figure 2a), RWP (Figure 2b), and RR (Figure 2c) increase with updraft speed. Additionally, an increase in aerosol concentration leads to a decrease in both the maximum RWP and RR. Furthermore, Figure 2d illustrates that increasing the updraft speed and decreasing the aerosol number density result in an earlier rain initiation time. The rain initiation time is defined as the time at which the specific rainwater content surpasses a chosen small threshold ($q_r = 10^{-8}$ g kg$^{-1}$). Generally, higher updraft amplitudes and lower aerosol number densities lead to earlier and more substantial rain formation. Note that similar behavior can be observed at other surface pressures, with less rain observed for higher surface pressures. These observations highlight the sensitivity of rain formation to the values of updraft speed and aerosol number density, suggesting that the microphysical processes governing rain formation are susceptible to certain parameters. These findings are consistent with the results of Hill et al. (2023), where they demonstrate the high sensitivity of rain initiation time and amount to specific parameters and different super-droplet implementations.

The simulations conducted with the KiD-1d model using the SDM serve as a benchmark for calibrating warm-rain bulk microphysics schemes. This data set encompasses a wide range of precipitation conditions, from instances with no rain formation to those with substantial rainfall, with a maximum RWP exceeding 1.6 kg m$^{-2}$ for

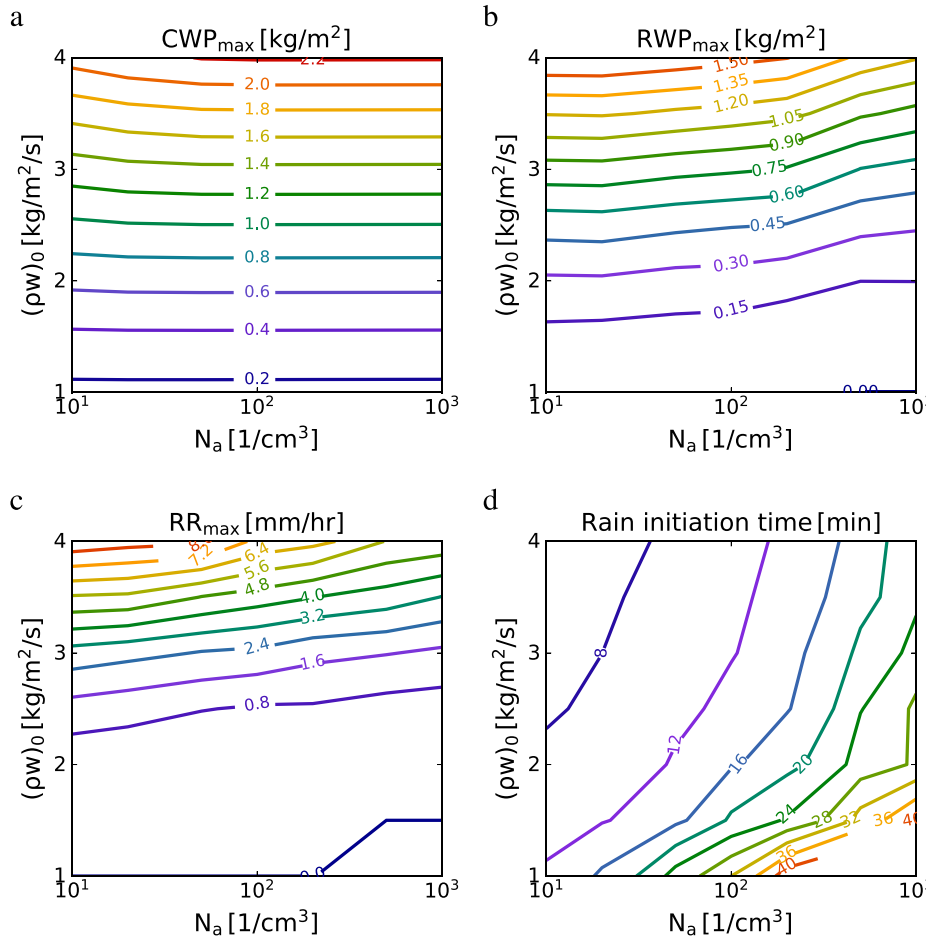


**Figure 2.** Sensitivity of outputs from the KiD-1d model using the super-droplet method to varying updraft momentum amplitude and initial aerosol number density. The panels display contours of (a) the maximum cloud water path $CWP_{max}$, (b) the maximum rainwater path $RWP_{max}$, (c) the maximum surface rain rate $RR_{max}$, and (d) the rain initiation time. The results are averaged over 100 simulations.

$p_0$ = 1,000 hPa. The observed sensitivities of cloud water content, rain initiation time, and rainwater content suggest that the data set represents diverse rates for microphysics processes, including condensation, auto-conversion, accretion, and rain evaporation. We anticipate that these sensitivities greatly contribute to the generalizability and effectiveness of the calibrated bulk microphysics schemes. However, it's important to note that the decoupling of microphysics from dynamics, particularly ignoring turbulence effects on collision-coalescence processes, is a limitation of this study. Additionally, the lack of lateral mixing and entrainment in the KiD-1d model represents a significant limitation. In a three-dimensional turbulent atmospheric environment, mixing and entrainment tend to broaden the droplet size distribution, impacting the efficiency of collision-coalescence and the formation of precipitation. The absence of these processes in our modeling framework means that the droplet size distributions produced might be narrower than those expected in a three-dimensional turbulent environment, influencing the modeled collision-coalescence and the precipitation formation. These limitations may introduce biases in the calibration results and negatively impact the performance of calibrated schemes in more complex setups like large eddy simulations or earth system models.

It is worth noting that the simulations in the KiD-1D model are not aimed at accurately representing the complex physics of a real precipitating cloud. Specifically, the KiD-1d model does not take into account turbulence or temperature fluctuations. Its design isolates microphysics from dynamics and thermodynamics, allowing for a focused study of microphysics phenomena. This isolation ensures that any variations observed in the results can be attributed solely to changes in the microphysics schemes being investigated. An alternative approach to decouple microphysical feedbacks from dynamics and thermodynamics is “microphysical piggybacking”

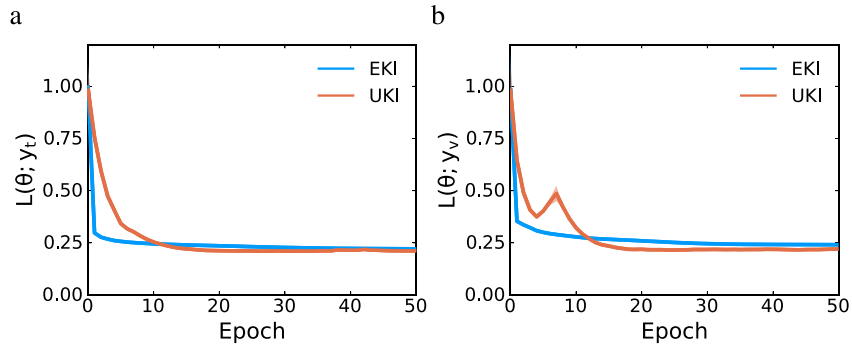


**Figure 3.** Variations of the loss function during calibration for the (a) training set and (b) validation set. Graphs in both panels are normalized by the loss of the model with the initial parameters to allow comparison.

(Grabowski, 2015; Grabowski & Morrison, 2016). The idea of piggybacking centers on the use of two sets of thermodynamic variables within a single simulation: one set actively interacts with and drives the simulation, while the second set, "piggybacking" the simulation, adapts to the flow dynamics without affecting it.

### 3.2. Calibration of a Bulk Scheme With the Library of Super-Droplet Simulations

In this subsection, we present the calibration results of the single-moment bulk microphysics scheme using the library of the SDM simulation results. For training the model, we use all SDM simulations with varying updraft amplitude and aerosol number density at the fixed surface pressure of $p_0 = 1{,}000$ hPa. In total, the training set contains $|C| = 49$ cases. From each individual simulation in a case, we extract mean values of specific cloud water content $\bar{q}_c$, rainwater content $\bar{q}_r$, and humidity $\bar{q}_v$ over intervals of 100 m and 10 min to use in the calibration process. We utilize a mini-batching technique, randomly selecting 6 configurations at a time for each calibration iteration, which facilitates effective and efficient training. Each epoch consists of 8 calibration iterations (for details see Section 2.4).

The validation set, on the other hand, is intentionally selected from configurations at a different ground-level pressure than the training set. This intentional selection allows us to assess whether the calibrated model can effectively capture simulations from a data set that is not used for training. Specifically, the validation set consists of simulations performed with the surface pressure $p_0 = 994$ hPa with updraft amplitudes of $(\rho w)_0 = [2, 3, 4]$ kg m$^{-2}$ s$^{-1}$ and aerosol number density $N_a = [50, 200]$ cm$^{-3}$. It is worth noting that the lower ground-level pressure of the validation set corresponds to approximately 0.5 K lower temperature. This leads to higher supersaturation and increased rain, providing a distinct data set for validation compared to the training data. As a result, it is unnecessary to modify the value of the updraft amplitudes and initial aerosol number densities in the validation set from those used in training.

It is important to note that aerosol-cloud interactions are treated differently between the reference SDM simulations and the bulk scheme model. While SDM provides a detailed representation of condensation processes, which resolves supersaturation-driven cloud condensation nuclei activation into cloud droplets, the bulk scheme simplifies this process by mapping aerosol concentration ($N_a$) to droplet concentration ($N_d$). In the context of our one-dimensional simulations, this mapping from $N_a$ to $N_d$ used in bulk parameterizations provides a reasonable approximation and does not significantly impact the calibration results.

Figure 3a shows the evolution of the configuration-averaged loss during calibrations for both EKI and UKI. Both EKI and UKI achieve a reduction of the loss to less than 25% of the initial loss observed with prior parameter values, demonstrating their effectiveness in identifying parameter sets that substantially improve model performance. Although calibration is continued for 50 epochs, significant loss reduction mainly occurs within the first 15 epochs, with EKI reducing the error more rapidly. It is important to note that the calibration process exclusively involves the training set to optimize the model parameters. The validation set, which comprises different atmospheric conditions not used in training, is employed solely for assessing the model's generalizability and performance. Figure 3b shows the evolution of the configuration-averaged loss based on the validation set for both EKI and UKI. When applying the calibrated model parameters to the validation set, we observe that the loss

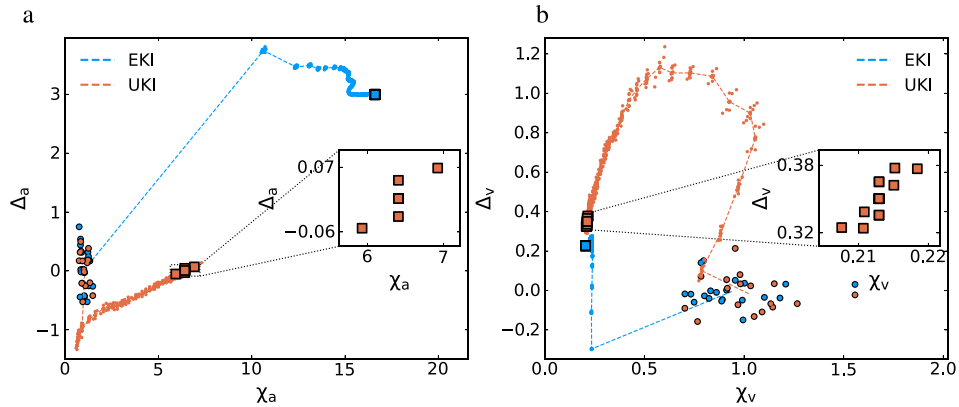


**Figure 4.** Evolution of (a) the two accretion coefficients, $\chi_a$ and $\Delta_a$, and (b) the two terminal velocity coefficients, $\chi_v$ and $\Delta_v$, during calibrations for both Ensemble Kalman Inversion (EKI) (dashed blue) and Unscented Kalman Inversion (UKI) (dashed orange). The initial ensembles of parameters are represented by blue circles (EKI) and orange circles (UKI), while the final ensembles of parameters are indicated by blue squares (EKI) and orange squares (UKI). Insets provide a zoomed-in view of the final parameter ensemble from UKI, illustrating the distribution as an indicator of parameter uncertainty. The final ensemble means for all parameters are given in Table 3.

reduction is almost equal to that of the training set, indicating that the calibrated model generalizes well to the precipitation conditions in the validation set.

Depending on the stochastic initialization of the parameter ensemble for EKI, EKI and UKI may converge to different sets of parameter values that minimize the mismatch between bulk method results and SDM simulations. This is demonstrated in Figure 4, which shows the evolution of the two accretion coefficients, $\chi_a$ and $\Delta_a$, as well as the two terminal velocity coefficients, $\chi_v$ and $\Delta_v$, by both EKI and UKI. While EKI and UKI converge to similar results for $\chi_v$ and $\Delta_v$, the evolution of the two accretion coefficients $\chi_a$ and $\Delta_a$ during the EKI and UKI calibrations shows significant differences, which indicates the convergence of EKI and UKI toward two distinct sets of parameters. The evolution of all parameters during the EKI and UKI calibrations is provided in Appendix B. The final values of all parameters obtained by EKI and UKI are provided in Table 3.

The main difference between the two parameter sets obtained by EKI and UKI is in the auto-conversion and accretion parameters. In the UKI set, the auto-conversion parameters, that control the auto-conversion time scale, are significantly larger than those in the EKI set. Consequently, the UKI set predicts larger auto-conversion time scales, leading to lower auto-conversion rates. However, this change is counterbalanced by the smaller values of the accretion coefficients, including $\Delta_a$, which governs the exponent of $q_r$ in the accretion process rate. With a smaller exponent, the accretion process yields larger rain production rates for small $q_r$ values, particularly in the early stages of rain production. Thus, larger accretion rates compensate for the smaller auto-conversion rates, resulting in comparable rain formations in the simulations.

**Table 3**
*Results of the Calibration of the Single-Moment Bulk Scheme by Ensemble Kalman Inversion and Unscented Kalman Inversion*

| Parameter name | Prior value | EKI optimal value | UKI optimal value |
|---|---|---|---|
| $\tau_{cond}$ | 10.0 s | 39.7 s | 35.0 s |
| $\tau_{acnv,\ 0}$ | $1.0 \times 10^3$ s | $13.4 \times 10^3$ s | $549.1 \times 10^3$ s |
| $\alpha_{acnv}$ | 1.0 | 0.52 | 2.09 |
| $\chi_v$ | 1.0 | 0.205 | 0.213 |
| $\Delta_v$ | 0.0 | 0.228 | 0.351 |
| $\chi_a$ | 1.0 | 16.61 | 6.41 |
| $\Delta_a$ | 0.0 | 3.00 | 0.01 |
| $b_{vent}$ | 0.53 | 0.98 | 1.48 |

*Note.* Columns represent parameter names, the prior parameter values, and the optimal parameter values from EKI and UKI calibrations. The optimal values are obtained by averaging the final ensembles of parameters.

Notably, the optimal auto-conversion time scale, $\tau_{acnv,\ 0}$, obtained by both EKI and UKI are larger than the auto-conversion time scale of 1,000 s documented in Grabowski and Smolarkiewicz (1996). This difference may be attributed to the fact that, unlike Grabowski and Smolarkiewicz (1996), we do not consider any auto-conversion threshold. Moreover, the exponent of $q_r$ in the accretion parameterization, $(\Delta_a + \Delta_v)/4 + 7/8$, is close to one for UKI optimal parameters. This is consistent with bulk schemes of Tripoli and Cotton (1980), Beheng (1994), and Seifert and Beheng (2006). In contrast, the exponent for EKI optimal parameters is relatively larger. Since both EKI and UKI achieve an approximate 75% reduction in loss, we accept both sets of parameters as valid calibrations for the bulk method. Incorporating detailed auto-conversion and accretion rate information in the training data could provide further insights and help obtain a unique set of optimal parameters.

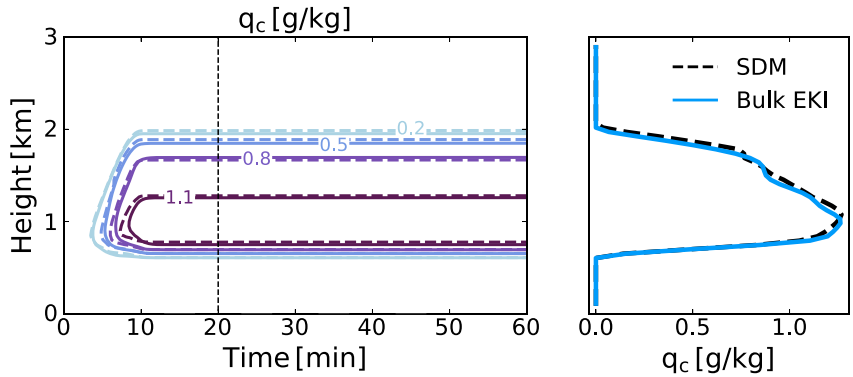


**Figure 5.** Comparison of the simulations of the KiD-1d model without collision processes using the super-droplet method (SDM) and the calibrated bulk method by Ensemble Kalman Inversion. Updraft amplitude is set to 3 kg $m^{-2}$ $s^{-1}$, and the initial aerosol number density is 100 $cm^{-3}$. The left panel shows height-time contours of specific cloud water content, while the right panel displays the specific cloud water content at $T = 20$ min. The results from both methods, the SDM and the calibrated bulk method, are in excellent agreement showing that the bulk scheme well captures the condensation process.

In addition to identifying optimal parameter values, UKI offers insights into parameter uncertainty bounds. We observe that the standard deviation of the parameter ensemble obtained by UKI defines a narrow range of parameters (see Figure B1). Remarkably, both the initial parameter values and the estimates from EKI fall outside these uncertainty bounds. This may arise from the low variability in the reference data set and the methodological assumptions of UKI, including its reliance on Gaussian approximations for parameter distributions. These assumptions might not fully represent the complexity and inherent nonlinearities of cloud microphysics, leading to the observed discrepancies between expected and observed parameter ranges. Despite these considerations, the uncertainty estimates from UKI provide valuable insights. They offer a quantifiable measure of confidence in the parameter estimates and illuminate correlations between parameters, indicating directions for model improvement.

In the simulation of the KiD-1d model, when precipitation processes are not included (condensation-only case), the only parameterized process is the condensation of water vapor into cloud water by Equation 9. Given the controlled dynamics and thermodynamics within the KiD-1D framework, we anticipate a close agreement between the simulation results of the condensation-only cases using the bulk method and SDM. Including precipitation in the simulations presents a more stringent challenge, testing the effectiveness of the bulk model's calibration under complex conditions. Despite this, the comparison of the bulk method and SDM for the condensation-only case serves as a key evaluation, validating the representation of condensation and water vapor advection processes within the bulk method against the SDM benchmark. Figure 5 shows results of the simulation of the KiD-1d model with $(\rho w)_0 = 3$ kg $m^{-2}$ $s^{-1}$, $N_a = 100$ $cm^{-3}$ and $p_0 = 1{,}000$ hPa in the condensation-only case by using the calibrated bulk method and SDM. Height-time contours of specific cloud water content $q_c$ and the profiles of $q_c$ at $t = 20$ min are compared. Note that in the condensation-only case the observed differences between the bulk method simulation with prior values and both EKI and UKI optimal values are relatively small. We thus only show the results of the EKI calibrated bulk method. The simulation results by the calibrated bulk method are in excellent agreement with the results of the SDM. This excellent agreement confirms the satisfactory performance of the implementation of condensation and water vapor advection in the bulk method simulations.

Figures 6 and 7 compare simulations using the SDM, the bulk method before training, and the calibrated bulk method by EKI and UKI. Figure 6 visualizes contours of specific cloud water content $q_c$ and specific rainwater content $q_r$ in height and time, while Figure 7 shows profiles of $q_c$ and $q_r$ at $t = 10$ min, $t = 20$ min, $t = 30$ min, and $t = 50$ min. As evidenced in these figures, the bulk method with the initial parameters underestimates the specific cloud water content and incorrectly predicts an early peak in specific rainwater content. These deviations suggest an overestimation of rain production and sedimentation rates in the bulk method before training. However, both EKI and UKI optimal parameters significantly improve the bulk method simulations with respect to the SDM results. After calibrations, the auto-conversion parameters $\tau_{acnv,\,0}$ and $\alpha_{acnv}$ increase, resulting in reduced auto-conversion rates. Additionally, the terminal velocity parameter $\chi_v$ decreases, leading to reduced sedimentation. On the other hand, the accretion parameter $\chi_a$ increases in both EKI and UKI calibrations. However, it is important

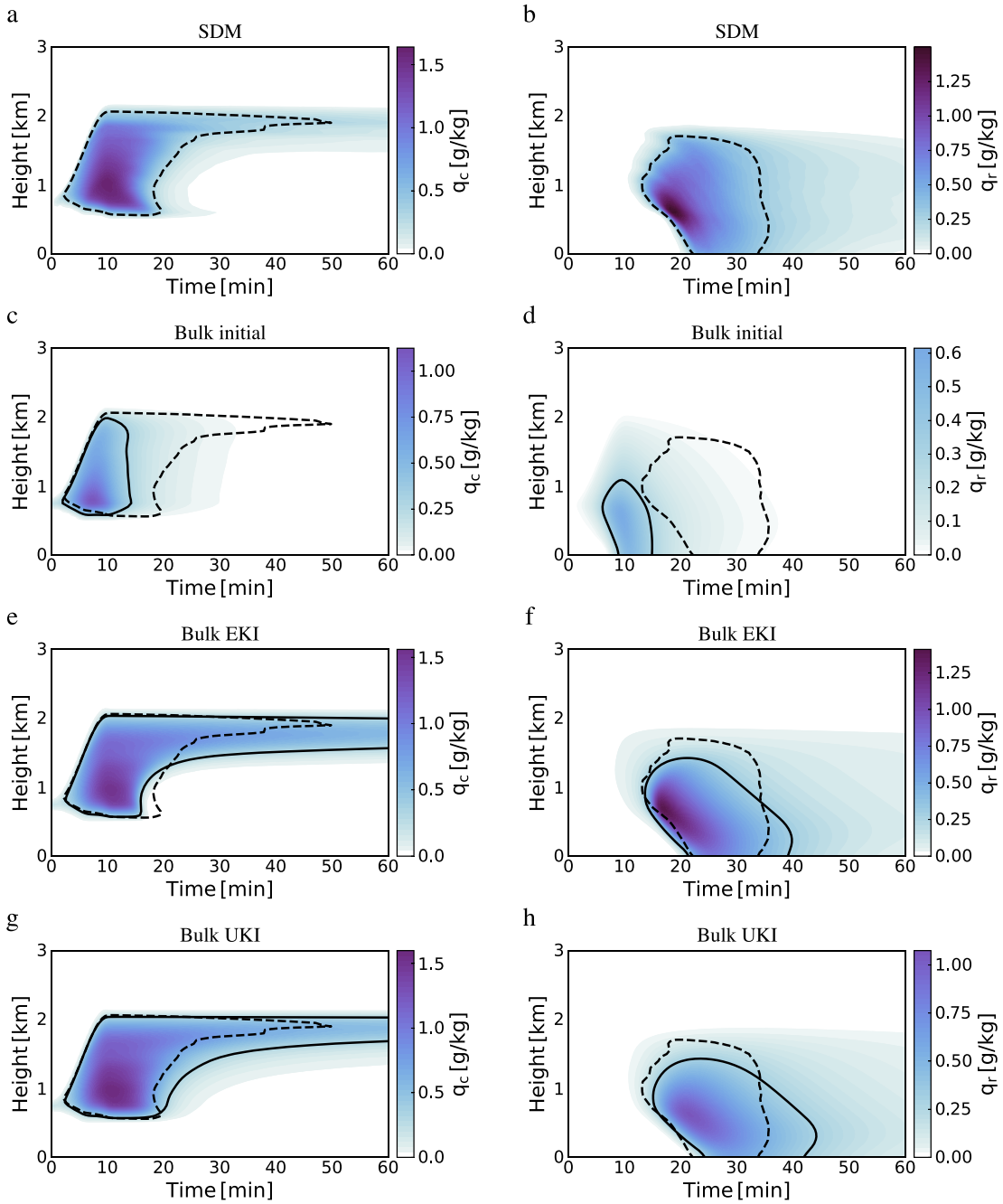


**Figure 6.** Comparison of the KiD-1d model simulations using the super-droplet method (SDM) and the bulk method. Height-time contours of specific cloud water content $q_c$ (left panels) and specific rainwater content $q_r$ (right panels) are compared for the simulations using the SDM (a and b), the bulk method with the initial parameters (c and d), and the calibrated method by Ensemble Kalman Inversion (e and f) and Unscented Kalman Inversion (g and h). Black solid lines indicate $q_c = 0.3$ g kg$^{-1}$ (left panels) and $q_r = 0.3$ g kg$^{-1}$ (right panels), while black dashed lines represent the same contour levels for the SDM results, overlaid on all panels for comparison. The simulations use $(\rho w)_0 = 3$ kg m$^{-2}$ s$^{-1}$, $N_a = 50$ cm$^{-3}$, and $p_0 = 994$ hPa. The SDM results are the average of 100 simulations.

to note that the accretion rate, which is influenced by sedimentation, is governed by the product $\chi_a \chi_v$. In the calibrated bulk method, this product slightly increases compared to that with the initial parameters. These parameter adjustments contribute to the overall decrease of rain formation and sedimentation, and the reasonable agreement of the calibrated bulk method, by both EKI and UKI, with the SDM results.

While the simulations using the calibrated bulk method by EKI and UKI yield similar overall results, there are differences in specific details. For example, the maximum specific rainwater content for the EKI calibrated bulk

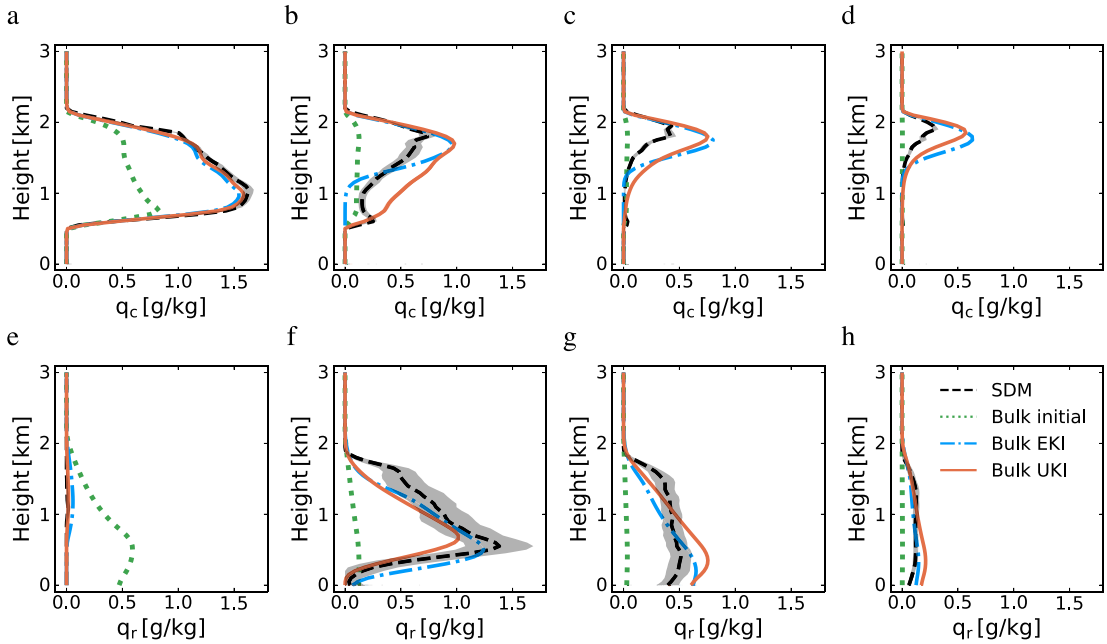


**Figure 7.** Solutions of the super-droplet method (SDM) and the bulk method with the initial and the calibrated parameters are compared. The specific cloud water content profiles (top panels) and specific rainwater content profiles (bottom panels) are shown at times $t = 10$ min (panels a and e), $t = 20$ min (panels b and f), $t = 30$ min (panels c and g) and $t = 50$ min (panels d and h). The calibrated bulk method results are obtained by evaluating the model using the ensemble means. For the SDM results, the dashed lines represent the average of 100 simulations, while the shadings visualize the variability, showing plus and minus one standard deviation.

method exceeds that for the UKI calibrated bulk method by more than 30%. Also, when $q_r$ for the SDM peaks ($t \sim 20$ min), the EKI calibrated bulk method underestimates $q_c$ close to the cloud base while the UKI calibrated bulk method overestimates it compared to SDM results. This observation suggests that the rain production rate for the EKI calibrated bulk method is overestimated while that for the UKI calibrated bulk method is underestimated. This is confirmed in Figure 8 where CWP, RWP and RR are visualized over time. The RWP for the SDM peaks slightly after that for the EKI calibrated bulk method and shortly before that for the UKI calibrated bulk method, indicating the overestimation of the rain production rate by the EKI calibrated bulk method and the underestimation of the rate by the UKI calibrated bulk method. The higher rain production rates predicted by the EKI calibrated bulk method occur around the peak of $q_r$, which corresponds to the period when accretion is the dominant rain formation process. This observation suggests that the EKI calibrated method predicts higher accretion rates for large values of $q_r$ compared to the UKI calibrated method. This difference in accretion rates can be attributed to the higher value of the accretion parameter $\chi_a$ in the EKI parameter set. Additionally, it is notable that the RR for the EKI calibrated bulk method is more than 30% higher than that for the UKI calibrated bulk method. The higher RR is due to the lower evaporation rate of the EKI calibrated bulk method (caused by smaller $b_{vent}$) than that of the UKI calibrated bulk method. These differences highlight the uncertainty associated with parameter values in the calibration process, emphasizing the need for further research to refine these parameters and enhance the reliability of simulation outcomes.

The bulk method before training incorrectly predicts an early RR due to the incorrect prediction of early rain production. The calibrated bulk methods by both EKI and UKI predict the timing of the RR very well. However, they fail to correctly predict the magnitude of the maximum RR. The significant error in the prediction of the maximum RR despite capturing $q_r$ well can be attributed to the inability of the single-moment bulk method to adequately predict the terminal velocity of particles. The poor representation of terminal velocity by the single-moment bulk scheme is inevitable as terminal velocity is simply a single-valued function of $q_r$ and the gravitational size sorting is not captured (Milbrandt & McTaggart-Cowan, 2010). The prediction of the maximum RR can be improved by using multi-moment bulk schemes with sedimentation rates that can capture gravitational size sorting.

Figure 9 presents a comparative overview of the maximum CWP, maximum RWP, maximum RR, and the timing of the maximum RR across all validation cases. Validation cases include various updraft amplitudes and aerosol

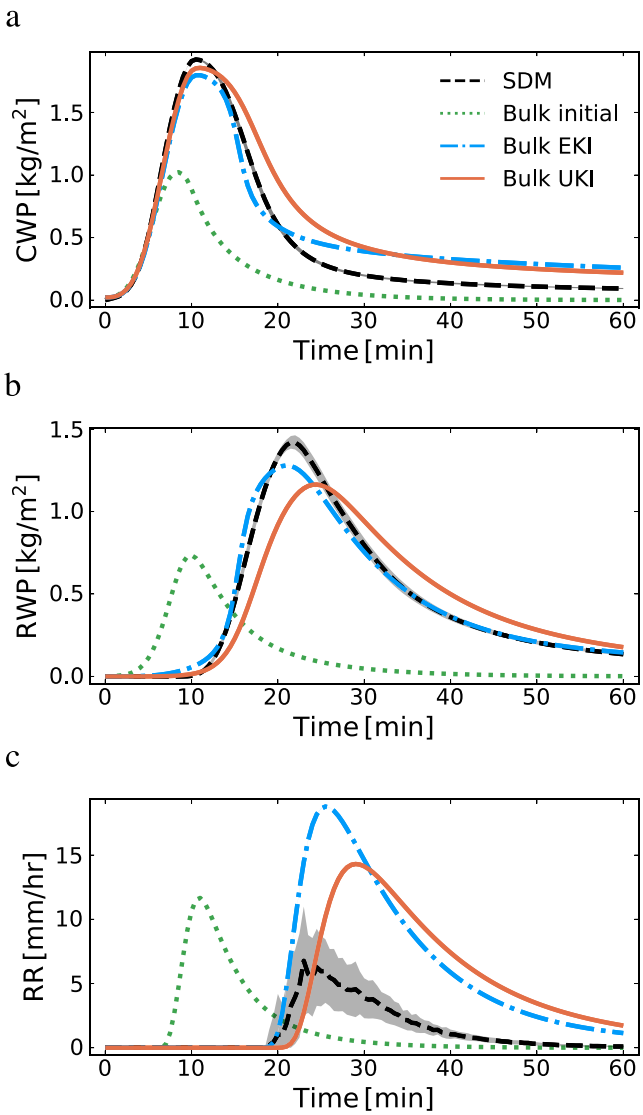


**Figure 8.** (a) Comparison of the cloud water path CWP, (b) rainwater path RWP, and (c) surface rain rate RR for simulations using the super-droplet method (SDM) (black dashed), the bulk method with the initial parameters (green dotted), and the calibrated bulk method by Ensemble Kalman Inversion (blue dash-dot) and Unscented Kalman Inversion (orange solid). The results of the calibrated bulk method are obtained by evaluating the bulk method with the ensemble mean. The SDM results represent the average of 100 simulations, and the profile variability is indicated by shading plus and minus one standard deviation.

number densities, with a surface pressure of 994 hPa, which corresponds to an 0.5 K colder temperature profile across the domain compared to the training set. Similar to the observations in the single validation case discussed earlier, the calibrated bulk methods by EKI and UKI consistently predict the maximum CWP, the maximum RWP, and the timing of the RR very well across all validation scenarios, showing the effectiveness of the calibrated models in replicating the microphysical processes. However, a recurring challenge observed across the validation set is the overestimation of the maximum RR by both calibrated methods when compared to the SDM, underscoring the limitations of the single-moment bulk scheme in capturing sedimentation accurately.

In addition to the maximum likelihood estimator, UKI provides correlations between model parameters. Figure 10a visualizes the correlation map between parameters of the single-moment bulk scheme obtained by the UKI calibration. For the employed training data set, the calibrated bulk scheme shows strong correlations between the two auto-conversion parameters $\tau_{acnv,\ 0}$ and $\alpha_{acnv}$, between the two accretion coefficients $\chi_a$ and $\Delta_a$, as well as between the two terminal velocity coefficients $\chi_v$ and $\Delta_v$. Also, both accretion coefficients are moderately anti-correlated with auto-conversion and terminal velocity coefficients.

The correlations between the two accretion coefficients and between the two terminal velocity coefficients can be attributed to the compensatory nature of these parameters in their corresponding process rate equations. Specifically, an increase in the scaling factor (e.g., $\chi_a$ or $\chi_v$) is accompanied by a corresponding increase in the exponent of $q_r$ (e.g., $\Delta_a$ or $\Delta_v$). The anti-correlations between the accretion and terminal velocity parameters arise from the direct effect of sedimentation on the accretion rate. The anti-correlation between the accretion coefficients and the auto-conversion parameters is due to the counterbalance between these two processes in the early stages of rain formation. The strong correlation between the two auto-conversion parameters suggests that as the initial number density $N_a$ increases, a greater adjustment in the auto-conversion process is required to maintain a balanced rain formation process.

Utilizing the correlation information provided by UKI can contribute to refining the parameterizations of the bulk method by identifying a smaller set of uncorrelated parameters for calibrations. For instance, the strong correlation between auto-conversion parameters suggests that training the model for only one of the two parameters might result in a similar reduction of the model-data mismatch as training for both parameters.

The parameter correlations derived from UKI are consistent with the differences between the optimal parameter sets obtained by EKI and UKI. In the set of UKI optimal parameters, both auto-conversion parameters are higher than those in the EKI set, while both accretion coefficients are lower and both terminal velocity coefficients are slightly higher. The parameter correlations and the consistent differences between the EKI and UKI optimal parameter sets suggest the existence of a range of parameters for which the model-data mismatch remains acceptably small. This is illustrated in Figures 10b and 10c, where contours of the configuration-averaged loss function are visualized for varying accretion parameters $\chi_a$ and $\Delta_a$, while other parameters are fixed at the EKI or UKI optimal values. As evidenced in this figure, the loss function value remains below 25% within a notably wide region in the space of $\chi_a$ and $\Delta_a$. These results demonstrate the existence of a continuous range of parameter combinations that yield satisfactory model performance, allowing for flexibility in selecting parameter values. The convergence to different points within this low-loss region of parameter space can be attributed to the distinct update rules of EKI and UKI, as well as differences in their initial parameter ensembles. Obtaining a unique set of parameters can be

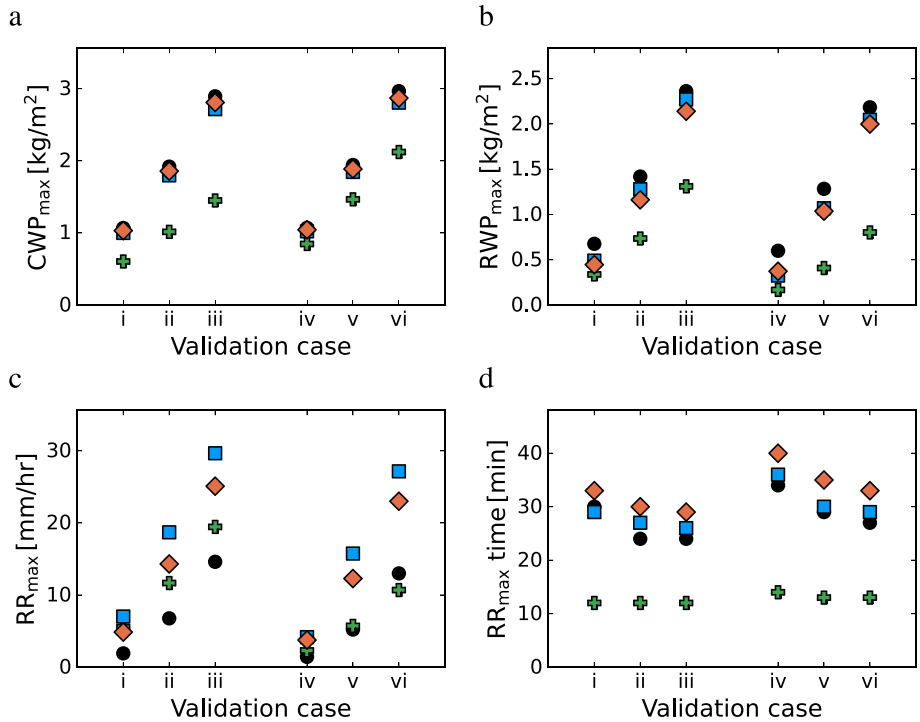


**Figure 9.** Comparison of simulation outcomes for (a) maximum cloud water path $CWP_{max}$, (b) maximum rainwater path $RWP_{max}$, (c) maximum surface rain rate $RR_{max}$, and (d) the timing of the maximum rain rate across all cases in the validation set. Results are shown for the super-droplet method (SDM) (black circles), the bulk method with initial parameters (green crosses), and the bulk method calibrated using Ensemble Kalman Inversion (blue squares) and Unscented Kalman Inversion (orange diamonds). The cases, numbered i to vi, differ by updraft amplitude ($(\rho w)_0$ in kg m$^{-2}$ s$^{-1}$) and aerosol number density ($N_a$ in cm$^{-3}$), as follows: case i: $(\rho w)_0 = 2$, $N_a = 50$; case ii: $(\rho w)_0 = 3$, $N_a = 50$; case iii: $(\rho w)_0 = 4$, $N_a = 50$; case iv: $(\rho w)_0 = 2$, $N_a = 200$; case v: $(\rho w)_0 = 3$, $N_a = 200$; and case vi: $(\rho w)_0 = 4$, $N_a = 200$. The surface pressure for the validation set is $p_0 = 994$ hPa, differing from the training set's surface pressure of $p_0 = 1{,}000$ hPa. The calibrated bulk method results are evaluated with the ensemble mean, while the SDM results are based on the average of 100 samples.

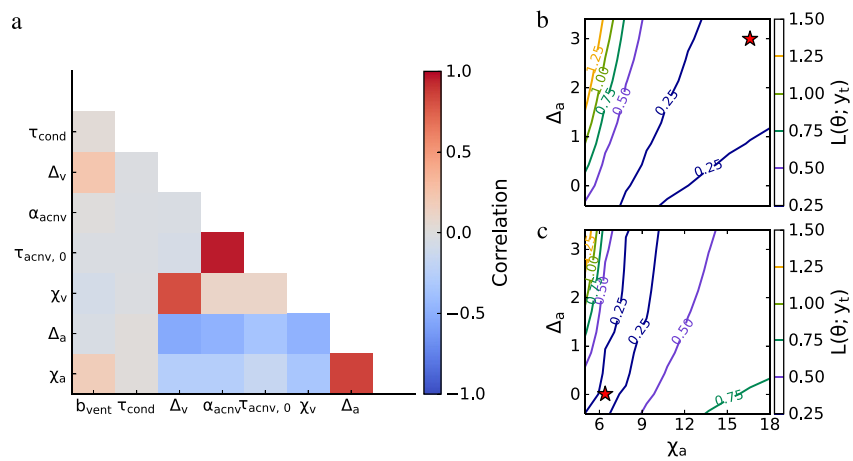


**Figure 10.** Parameter correlations estimated using the Unscented Kalman Inversion (UKI) method (a), and contours of the loss function $L(\theta; y_t)$ for varying accretion parameters $\chi_a$ and $\Delta_a$, while keeping other parameters fixed at the Ensemble Kalman Inversion (EKI) (b) and UKI (c) optimal values. The markers indicate the optimal values of the accretion parameters obtained by EKI (b) and UKI (c). The loss values are normalized by the value of the loss evaluated for the bulk model with the initial parameters.

achieved by providing additional constraints for parameter estimation through incorporating detailed information about auto-conversion and accretion processes in the training data. While SDM does not directly output auto-conversion and accretion rates, it is possible to infer these rates indirectly from the comprehensive collision-coalescence data available within SDM simulations. By leveraging such information, it may become possible to refine the parameterizations of the bulk method and enhance the model's capability to capture the underlying dynamics. The investigation into incorporating auto-conversion and accretion process rates into the parameterization of the bulk model is left for future research.

## 4. Summary and Conclusion

The aim of this study was to improve the accuracy of the representation of cloud and precipitation processes within bulk schemes. We presented a calibration framework for training warm-rain bulk microphysics schemes by using high-fidelity super-droplet simulations. The calibration framework uses ensemble Kalman methods for training the models, including EKI and UKI. Calibrations are carried out by leveraging simulations of the KiD-1d model, a one-dimensional rain-shaft model that has been widely used for studying microphysics schemes. In this model, the updraft and the temperature profile are prescribed so that any variation in the results can only be attributed to changes in the employed microphysics scheme.

To benchmark the performance of the bulk methods, we generated a library of super-droplet simulations of a rain shaft model. Simulations were carried out for different updraft amplitudes, initial aerosol number density, and surface air pressure to provide a wide range of precipitation conditions for comparing and evaluating bulk microphysics schemes.

Our results demonstrate the effectiveness of the calibration framework by applying it to a single-moment microphysics model. While calibrations by EKI and UKI result in two different sets of parameters, the calibrated bulk method by both EKI and UKI shows a significant reduction in model error with respect to the super-droplet simulations. Specifically, the prediction of cloud and rain profiles showed excellent agreement with the reference simulations. However, while the timing of the surface precipitation rate showed improvement, the magnitude of the maximum RR was overpredicted by the single-moment bulk scheme. This finding emphasizes the need for further research to capture the surface precipitation rate more accurately, particularly by exploring the potential of higher-moment schemes that can represent the gravitational size sorting of particles.

While our results demonstrate the efficacy of our calibration approach within a one-dimensional framework, we acknowledge that simplifications in our simulation setup, such as the lack of lateral mixing and entrainment which causes narrower PSD, might affect the outcomes. A comprehensive validation of the calibrated model's generalizability, particularly to more complex and realistic atmospheric conditions, would therefore benefit from the application of three-dimensional simulations. The extension to three-dimensional simulations is highlighted as an important direction for future work.

In this study, the application of ensemble Kalman methods (EKI and UKI) for calibrating a single-moment warm-rain bulk scheme by using SDM simulations has revealed two distinct yet effective parameter sets, illustrating the phenomenon of equifinality in model calibration. These sets, while not equivalent demonstrate the model's flexibility and the presence of compensation effects where diverse parameter sets achieve similar model performance. This outcome is further supported by parameter correlation analysis by UKI, which suggests the existence of a continuous spectrum of viable parameter combinations. The insights from the correlation analysis help us to understand the interdependencies between parameters, indicating that multiple pathways can lead to comparable improvements in model performance. This analysis underscores the importance of further refining the model by incorporating independent constraints on microphysical processes, including detailed information from SDM simulations on processes like auto-conversion and accretion, to reduce compensating parameter uncertainties. Future research will focus on integrating such detailed process rates into the bulk scheme's parameterization, aiming to identify more constrained and physically realistic parameter sets that improve model accuracy and reduce the ambiguity associated with equifinality. This work underscores the complexity of microphysics simulation and the ongoing need for comprehensive strategies to refine model parameterizations within the inherent limitations of observational and simulation data.

Our study highlights the potential of calibrating classic parameterizations of microphysics using high-fidelity super-droplet simulations. Although super-droplet techniques are still in their early stages and pose potential limitations in capturing the entirety of the underlying physical phenomena (Hill et al., 2023; Morrison et al., 2020), leveraging the valuable insights obtained from these simulations can enhance classic microphysics parameterizations. Unlike observational data, these simulations allow us to disentangle microphysics from other dynamics and calibrate microphysics processes in isolation from their feedbacks with atmospheric flows. However, with this decoupling, aspects of the cloud system evolution sensitive to these feedbacks cannot serve as observational constraints. Despite this limitation, the ability to isolate microphysics offers a significant advantage, enabling us to explore and refine microphysics parameterizations in a controlled manner, which would be challenging even with abundant laboratory or observational data. Utilizing super-droplet simulations is a promising approach to improve microphysics parameterizations, particularly in regions where clouds show strong sensitivity to microphysics parameters. Further research in this direction is needed to explore the full potential and capability of the super-droplet simulations in improving the accuracy of classic parameterizations of cloud microphysics.

## Appendix A: Result Independence From Numerical Values

Figure A1 compares SDM simulations of the KiD-1d model with $(\rho w)_0 = 3$ kg m$^{-2}$ s$^{-1}$, $N_a = 100$ cm$^{-3}$ and $p_0 = 1{,}000$ hPa for different numerical setups. The reference simulation with an average of $N_{sd} = 512$ super-droplets per grid box, $dz = 50$ m and $dt = 5$ s is compared against simulations with doubled number of super-droplets, halved grid spacing, and halved time step. The results are in excellent agreement, indicating the independence of the reference simulation from specific numerical values.

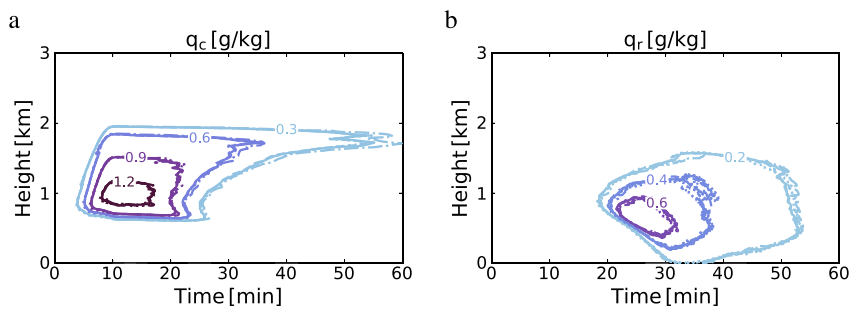


**Figure A1.** Comparison of KiD-1d model simulations using the super-droplet method with different numerical settings. Height-time contours of specific content for cloud water (panel a) and rain (panel b) are shown. The solid contour lines represent the simulation with $N_{sd} = 512$ super-droplets, grid spacing of $dz = 50$ m, and time steps of $dt = 5$ s. This simulation is compared with simulations using doubled number of super-droplets (dashed), halved grid spacing (dashdot) and halved time steps (dot). The averages of 100 simulations for each set of numerical settings are shown. The excellent agreement of results indicates that the KiD-1d model simulations are insensitive to the numerical settings used.

## Appendix B: Parameter Evolution in EKI and UKI Calibrations

Figure B1 displays the evolution of all calibrated parameters during the calibration of the single-moment bulk scheme using EKI and UKI methods. The calibrated parameters include accretion coefficients, terminal velocity coefficients, auto-conversion coefficients, condensation time scale, and evaporation coefficient. While EKI and UKI show comparable final converged values for the terminal velocity coefficients ($\chi_v$ and $\Delta_v$) and the condensation time scale ($\tau_{cond}$), the final converged values of the remaining parameters by EKI and UKI are significantly different. Note that the low uncertainty bounds in Figure B1 may be attributed to the low variability in the reference SDM simulations. After temporal and spatial averaging, the maximum standard deviation across samples typically ranges from 5% to 10% of the maximum field values, influencing the breadth of uncertainty bounds that can be derived through UKI.

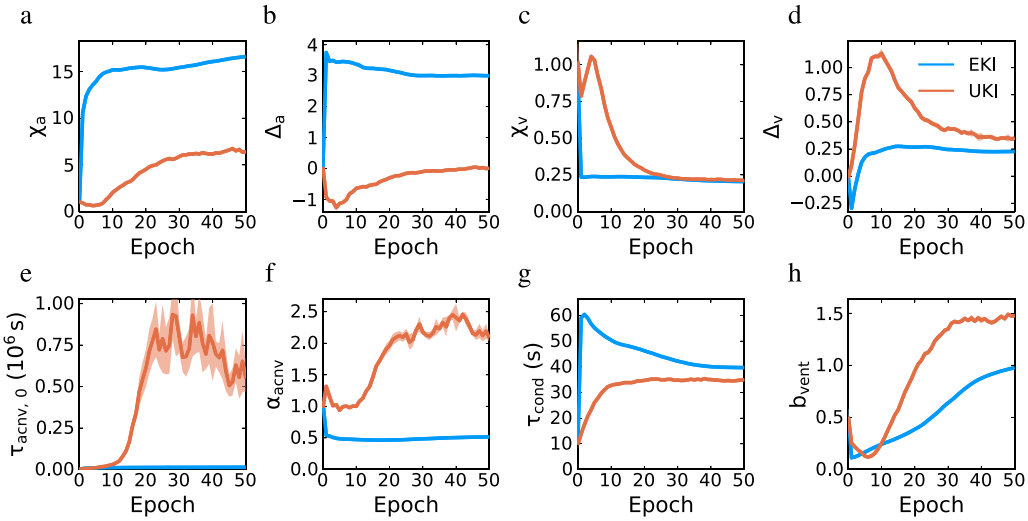


**Figure B1.** (a) Parameter evolutions of the accretion coefficient $\chi_a$ and (b) $\Delta_a$, (c) terminal velocity coefficient $\chi_v$ and (d) $\Delta_v$, (e) auto-conversion coefficient $\tau_{acnv,\,0}$ and (f) $\alpha_{acnv}$, (g) condensation time scale $\tau_{cond}$, and (h) evaporation coefficient $b_{vent}$ during calibrations using Ensemble Kalman Inversion (blue) and Unscented Kalman Inversion (UKI) (red). The parameter uncertainty obtained from UKI is illustrated by shadings, indicating plus and minus one standard deviation of the parameter ensemble.

## Conflict of Interest

The authors declare no conflicts of interest relevant to this study.

## Data Availability Statement

The library of super-droplet simulations is available at https://doi.org/10.5281/zenodo.8336442 (Azimi, de Jong, et al., 2023). These simulations were generated using PySDM version 2.15 (Bartman, Bulenok, et al., 2022; de Jong et al., 2023), which is accessible on Github at https://github.com/open-atmos/PySDM. The source code for the calibration pipeline can be found at https://doi.org/10.5281/zenodo.8362305 (Azimi, Jaruga, & de Jong, 2023). The bulk microphysics scheme used in this study is implemented in the Julia package CloudMicrophysics.jl version 0.13.3 (CliMA, 2023), available on Github at https://github.com/CliMA/CloudMicrophysics.jl. For the calibrations, we used the Julia package EnsembleKalmanProcesses.jl version 1.1 (Dunbar, Lopez-Gomez, et al., 2022), available on Github at https://github.com/CliMA/EnsembleKalmanProcesses.jl.

**Acknowledgments**
The authors thank the reviewers for their insightful comments and suggestions, which have significantly contributed to improving this manuscript. Sajjad Azimi acknowledges support by the Swiss National Science Foundation (SNSF, Grant P500PN_202876). Sylwester Arabas acknowledges support by the Polish National Science Centre (NCN, Grant 2020/39/D/ST10/01220). This research was additionally supported by the generosity of Eric and Wendy Schmidt by recommendation of the Schmidt Futures program and by the U.S. National Science Foundation (Grant AGS-1835860).

## References

Andrejczuk, M., Grabowski, W. W., Reisner, J., & Gadian, A. (2010). Cloud-aerosol interactions for boundary layer stratocumulus in the Lagrangian Cloud Model. *Journal of Geophysical Research*, *115*(D22), D22214. https://doi.org/10.1029/2010JD014248

Azimi, S., de Jong, E., Jaruga, A., & Arabas, S. (2023). Super-droplet simulations of a 1D rain shaft model [Dataset]. *Zenodo*. https://doi.org/10.5281/zenodo.8336442

Azimi, S., Jaruga, A., & de Jong, E. (2023). Kinematic1D (Version 0.3.4) [Software]. *Zenodo*. https://doi.org/10.5281/zenodo.8362305

Bartman, P., Banaśkiewicz, J., Drenda, S., Manna, M., Olesik, M. A., Rozwoda, P., et al. (2022). PyMPDATA v1: Numba-accelerated implementation of MPDATA with examples in Python, Julia and Matlab. *Journal of Open Source Software*, *7*(77), 3896. https://doi.org/10.21105/joss.03896

Bartman, P., Bulenok, O., Górski, K., Jaruga, A., Łazarski, G., Olesik, M. A., et al. (2022). PySDM v1: Particle-based cloud modeling package for warm-rain microphysics and aqueous chemistry. *Journal of Open Source Software*, *7*(72), 3219. https://doi.org/10.21105/joss.03219

Beheng, K. (1994). A parameterization of warm cloud microphysical conversion processes. *Atmospheric Research*, *33*(1–4), 193–206. https://doi.org/10.1016/0169-8095(94)90020-5

Berry, E. X. (1967). Cloud droplet growth by collection. *Journal of the Atmospheric Sciences*, *24*(6), 688–701. https://doi.org/10.1175/1520-0469(1967)024⟨0688:CDGBC⟩2.0.CO;2

Bieli, M., Dunbar, O. R. A., de Jong, E. K., Jaruga, A., Schneider, T., & Bischoff, T. (2022). An efficient Bayesian approach to learning droplet collision kernels: Proof of concept using "Cloudy," a new n-moment bulk microphysics scheme. *Journal of Advances in Modeling Earth Systems*, *14*(8), e2022MS002994. https://doi.org/10.1029/2022MS002994

Bocquet, M., Pires, C. A., & Wu, L. (2010). Beyond Gaussian statistical modeling in geophysical data assimilation. *Monthly Weather Review*, *138*(8), 2997–3023. https://doi.org/10.1175/2010MWR3164.1

Cleary, E., Garbuno-Inigo, A., Lan, S., Schneider, T., & Stuart, A. M. (2021). Calibrate, emulate, sample. *Journal of Computational Physics*, *424*, 109716. https://doi.org/10.1016/j.jcp.2020.109716

CliMA. (2023). CloudMicrophysics.jl (Version 0.13.3) [Software]. *Github*. Retrieved from https://github.com/CliMA/CloudMicrophysics.jl

de Jong, E. K., Singer, C. E., Azimi, S., Bartman, P., Bulenok, O., Derlatka, K., et al. (2023). New developments in PySDM and PySDM-examples v2: Collisional breakup, immersion freezing, dry aerosol initialization, and adaptive time-stepping. *Journal of Open Source Software*, *8*(84), 4968. https://doi.org/10.21105/joss.04968

Dunbar, O. R. A., Garbuno-Inigo, A., Schneider, T., & Stuart, A. M. (2021). Calibration and uncertainty quantification of convective parameters in an Idealized GCM. *Journal of Advances in Modeling Earth Systems*, *13*(9), e2020MS002454. https://doi.org/10.1029/2020MS002454

Dunbar, O. R. A., Howland, M. F., Schneider, T., & Stuart, A. M. (2022). Ensemble-based experimental design for targeting data acquisition to inform climate models. *Journal of Advances in Modeling Earth Systems*, *14*(9), e2022MS002997. https://doi.org/10.1029/2022MS002997

Dunbar, O. R. A., Lopez-Gomez, I., Garbuno-Iñigo, A., Huang, D. Z., Bach, E., & Wu, J.-L. (2022). EnsembleKalmanProcesses.jl: Derivative-free ensemble-based model calibration. *Journal of Open Source Software*, *7*(80), 4869. https://doi.org/10.21105/joss.04869

Gettelman, A., Gagne, D. J., Chen, C., Christensen, M. W., Lebo, Z. J., Morrison, H., & Gantos, G. (2021). Machine learning the warm rain process. *Journal of Advances in Modeling Earth Systems*, *13*(2), e2020MS002268. https://doi.org/10.1029/2020MS002268

Grabowski, W. W. (1998). Toward cloud resolving modeling of large-scale tropical circulations: A simple cloud microphysics parameterization. *Journal of the Atmospheric Sciences*, *55*(21), 3283–3298. https://doi.org/10.1175/1520-0469(1998)055⟨3283:TCRMOL⟩2.0.CO;2

Grabowski, W. W. (2015). Untangling microphysical impacts on deep convection applying a novel modeling methodology. *Journal of the Atmospheric Sciences*, *72*(6), 2446–2464. https://doi.org/10.1175/JAS-D-14-0307.1

Grabowski, W. W., & Morrison, H. (2016). Untangling microphysical impacts on deep convection applying a novel modeling methodology. Part II: Double-moment microphysics. *Journal of the Atmospheric Sciences*, *73*(9), 3749–3770. https://doi.org/10.1175/JAS-D-15-0367.1

Grabowski, W. W., Morrison, H., Shima, S.-I., Abade, G. C., Dziekan, P., & Pawlowska, H. (2019). Modeling of cloud microphysics: Can we do better? *Bulletin of the American Meteorological Society*, *100*(4), 655–672. https://doi.org/10.1175/BAMS-D-18-0005.1

Grabowski, W. W., & Smolarkiewicz, P. K. (1996). Two-time-level semi-Lagrangian modeling of precipitating clouds. *Monthly Weather Review*, *124*(3), 487–497. https://doi.org/10.1175/1520-0493(1996)124⟨0487:TTLSLM⟩2.0.CO;2

Hill, A. A., Lebo, Z. J., Andrejczuk, M., Arabas, S., Dziekan, P., Field, P., et al. (2023). Toward a numerical benchmark for warm rain processes. *Journal of the Atmospheric Sciences*, *80*(5), 1329–1359. https://doi.org/10.1175/JAS-D-21-0275.1

Huang, D. Z., Schneider, T., & Stuart, A. M. (2022). Iterated Kalman methodology for inverse problems. *Journal of Computational Physics*, *463*, 111262. https://doi.org/10.1016/j.jcp.2022.111262

Igel, A. L., Morrison, H., Santos, S. P., & van Lier-Walqui, M. (2022). Limitations of separate cloud and rain categories in parameterizing collision-coalescence for bulk microphysics schemes. *Journal of Advances in Modeling Earth Systems*, *14*(6), e2022MS003039. https://doi.org/10.1029/2022MS003039

Iglesias, M. A., Law, K. J. H., & Stuart, A. M. (2013). Ensemble Kalman methods for inverse problems. *Inverse Problems*, *29*(4), 045001. https://doi.org/10.1088/0266-5611/29/4/045001

Kessler, E. (1969). On the distribution and continuity of water substance in atmospheric circulations. In *On the distribution and continuity of water substance in atmospheric circulations* (pp. 1–84). American Meteorological Society. https://doi.org/10.1007/978-1-935704-36-2{_}1

Khain, A. P., Beheng, K. D., Heymsfield, A., Korolev, A., Krichak, S. O., Levin, Z., et al. (2015). Representation of microphysical processes in cloud-resolving models: Spectral (bin) microphysics versus bulk parameterization. *Reviews of Geophysics*, *53*(2), 247–322. https://doi.org/10.1002/2014RG000468

Khairoutdinov, M., & Kogan, Y. (2000). A new cloud physics parameterization in a large-eddy simulation model of marine stratocumulus. *Monthly Weather Review*, *128*(1), 229–243. https://doi.org/10.1175/1520-0493(2000)128⟨0229:ANCPPI⟩2.0.CO;2

Kogan, Y. (2013). A cumulus cloud microphysics parameterization for cloud-resolving models. *Journal of the Atmospheric Sciences*, *70*(5), 1423–1436. https://doi.org/10.1175/JAS-D-12-0183.1

Kogan, Y., & Belochitski, A. (2012). Parameterization of cloud microphysics based on full integral moments. *Journal of the Atmospheric Sciences*, *69*(7), 2229–2242. https://doi.org/10.1175/JAS-D-11-0268.1

Korolev, A. V., & Mazin, I. P. (2003). Supersaturation of water vapor in clouds. *Journal of the Atmospheric Sciences*, *60*(24), 2957–2974. https://doi.org/10.1175/1520-0469(2003)060⟨2957:SOWVIC⟩2.0.CO;2

Kovachki, N. B., & Stuart, A. M. (2019). Ensemble Kalman inversion: A derivative-free technique for machine learning tasks. *Inverse Problems*, *35*(9), 095005. https://doi.org/10.1088/1361-6420/ab1c3a

Li, M., Zhang, T., Chen, Y., & Smola, A. J. (2014). Efficient mini-batch training for stochastic optimization. In *Proceedings of the 20th ACM SIGKDD International Conference on Knowledge Discovery and Data Mining* (pp. 661–670). ACM. https://doi.org/10.1145/2623330.2623612

Liu, Y., & Daum, P. H. (2004). Parameterization of the autoconversion process. Part I: Analytical formulation of the Kessler-type parameterizations. *Journal of the Atmospheric Sciences*, *61*(13), 1539–1548. https://doi.org/10.1175/1520-0469(2004)061⟨1539:POTAPI⟩2.0.CO;2

Lohmann, U., Lüönd, F., & Mahrt, F. (2016). *An introduction to clouds*. Cambridge University Press. https://doi.org/10.1017/CBO9781139087513

Lopez-Gomez, I., Christopoulos, C., Langeland Ervik, H. L., Dunbar, O. R. A., Cohen, Y., & Schneider, T. (2022). Training physics-based machine-learning parameterizations with gradient-free ensemble Kalman methods. *Journal of Advances in Modeling Earth Systems*, *14*(8), e2022MS003105. https://doi.org/10.1029/2022MS003105

Marshall, J. S., & Palmer, W. M. K. (1948). The distribution of raindrops with size. *Journal of Meteorology*, *5*(4), 165–166. https://doi.org/10.1175/1520-0469(1948)005⟨0165:TDORWS⟩2.0.CO;2

Milbrandt, J. A., & McTaggart-Cowan, R. (2010). Sedimentation-induced errors in bulk microphysics schemes. *Journal of the Atmospheric Sciences*, *67*(12), 3931–3948. https://doi.org/10.1175/2010JAS3541.1

Milbrandt, J. A., & Yau, M. K. (2005). A multimoment bulk microphysics parameterization. Part I: Analysis of the role of the spectral shape parameter. *Journal of the Atmospheric Sciences*, *62*(9), 3051–3064. https://doi.org/10.1175/JAS3534.1

Morrison, H., & Grabowski, W. W. (2007). Comparison of bulk and bin warm-rain microphysics models using a kinematic framework. *Journal of the Atmospheric Sciences*, *64*(8), 2839–2861. https://doi.org/10.1175/JAS3980

Morrison, H., & Milbrandt, J. A. (2015). Parameterization of cloud microphysics based on the prediction of bulk ice particle properties. Part I: Scheme description and idealized tests. *Journal of the Atmospheric Sciences*, *72*(1), 287–311. https://doi.org/10.1175/JAS-D-14-0065.1

Morrison, H., van Lier-Walqui, M., Fridlind, A. M., Grabowski, W. W., Harrington, J. Y., Hoose, C., et al. (2020). Confronting the challenge of modeling cloud and precipitation microphysics. *Journal of Advances in Modeling Earth Systems*, *12*(8), e2019MS001689. https://doi.org/10.1029/2019MS001689

Morrison, H., van Lier-Walqui, M., Kumjian, M. R., & Prat, O. P. (2019). A Bayesian approach for statistical–physical bulk parameterization of rain microphysics. Part I: Scheme description. *Journal of the Atmospheric Sciences*, *77*(3), 1019–1041. https://doi.org/10.1175/JAS-D-19-0070.1

Noh, Y., Oh, D., Hoffmann, F., & Raasch, S. (2018). A cloud microphysics parameterization for shallow cumulus clouds based on Lagrangian cloud model simulations. *Journal of the Atmospheric Sciences*, *75*(11), 4031–4047. https://doi.org/10.1175/JAS-D-18-0080.1

Ott, E., Hunt, B. R., Szunyogh, I., Zimin, A. V., Kostelich, E. J., Corazza, M., et al. (2004). A local ensemble Kalman filter for atmospheric data assimilation. *Tellus A: Dynamic Meteorology and Oceanography*, *56*(5), 415. https://doi.org/10.3402/tellusa.v56i5.14462

Posselt, D. J. (2016). A Bayesian examination of deep convective squall-line sensitivity to changes in cloud microphysical parameters. *Journal of the Atmospheric Sciences*, *73*(2), 637–665. https://doi.org/10.1175/JAS-D-15-0159.1

Posselt, D. J., & Vukicevic, T. (2010). Robust characterization of model physics uncertainty for simulations of deep moist convection. *Monthly Weather Review*, *138*(5), 1513–1535. https://doi.org/10.1175/2009MWR3094.1

Riechelmann, T., Noh, Y., & Raasch, S. (2012). A new method for large-eddy simulations of clouds with Lagrangian droplets including the effects of turbulent collision. *New Journal of Physics*, *14*(6), 065008. https://doi.org/10.1088/1367-2630/14/6/065008

Schrom, R. S., van Lier-Walqui, M., Kumjian, M. R., Harrington, J. Y., Jensen, A. A., & Chen, Y.-S. (2021). Radar-based Bayesian estimation of ice crystal growth parameters within a microphysical model. *Journal of the Atmospheric Sciences*, *78*(2), 549–569. https://doi.org/10.1175/JAS-D-20-0134.1

Seifert, A., & Beheng, K. D. (2006). A two-moment cloud microphysics parameterization for mixed-phase clouds. Part 1: Model description. *Meteorology and Atmospheric Physics*, *92*(1–2), 45–66. https://doi.org/10.1007/s00703-005-0112-4

Shima, S., Kusano, K., Kawano, A., Sugiyama, T., & Kawahara, S. (2009). The super-droplet method for the numerical simulation of clouds and precipitation: A particle-based and probabilistic microphysics model coupled with a non-hydrostatic model. *Quarterly Journal of the Royal Meteorological Society*, *135*(642), 1307–1320. https://doi.org/10.1002/qj.441

Shipway, B. J., & Hill, A. A. (2012). Diagnosis of systematic differences between multiple parametrizations of warm rain microphysics using a kinematic framework. *Quarterly Journal of the Royal Meteorological Society*, *138*(669), 2196–2211. https://doi.org/10.1002/qj.1913

Tao, W. K., Chen, J. P., Li, Z., Wang, C., & Zhang, C. (2012). Impact of aerosols on convective clouds and precipitation. *Reviews of Geophysics*, *50*(2), RG2001. https://doi.org/10.1029/2011RG000369

Tong, X. T., & Morzfeld, M. (2023). Localized ensemble Kalman inversion. *Inverse Problems*, *39*(6), 064002. https://doi.org/10.1088/1361-6420/accb08

Tripoli, G. J., & Cotton, W. R. (1980). A numerical investigation of several factors contributing to the observed variable intensity of deep convection over south Florida. *Journal of Applied Meteorology*, *19*(9), 1037–1063. https://doi.org/10.1175/1520-0450(1980)019⟨1037:ANIOSF⟩2.0.CO;2

van Lier-Walqui, M., Morrison, H., Kumjian, M. R., Reimel, K. J., Prat, O. P., Lunderman, S., & Morzfeld, M. (2020). A Bayesian approach for statistical–physical bulk parameterization of rain microphysics. Part II: Idealized Markov chain Monte Carlo experiments. *Journal of the Atmospheric Sciences*, *77*(3), 1043–1064. https://doi.org/10.1175/JAS-D-19-0071.1

Xiao, H., Wu, J.-L., Wang, J.-X., Sun, R., & Roy, C. (2016). Quantifying and reducing model-form uncertainties in Reynolds-averaged Navier–Stokes simulations: A data-driven, physics-informed Bayesian approach. *Journal of Computational Physics*, *324*, 115–136. https://doi.org/10.1016/j.jcp.2016.07.038

Zeng, X., & Li, X. (2020). A two-moment bulk parameterization of the drop collection growth in warm clouds. *Journal of the Atmospheric Sciences*, *77*(3), 797–811. https://doi.org/10.1175/JAS-D-19-0015.1